Inorganic Chemistry

Forum Article

pubs.acs.org/IC

Characterization of the Bridged Hyponitrite Complex {[Fe(OEP)]$_2$(μ-N_2O_2)}: Reactivity of Hyponitrite Complexes and Biological Relevance

Timothy C. Berto,[†] Nan Xu,[‡] Se Ryeon Lee,[†] Anne J. McNeil,[†] E. Ercan Alp,[§] Jiyong Zhao,[§] George B. Richter-Addo,*[,‡] and Nicolai Lehnert*[,†]

[†]Department of Chemistry and Department of Biophysics, University of Michigan, 930 N. University Avenue, Ann Arbor, Michigan 48109, United States

[‡]Department of Chemistry and Biochemistry, University of Oklahoma, 101 Stephenson Parkway, Norman, Oklahoma 73019, United States

[§]Argonne National Laboratory, APS/XFD, 431/D003, Argonne, Illinois 60439, United States

Supporting Information

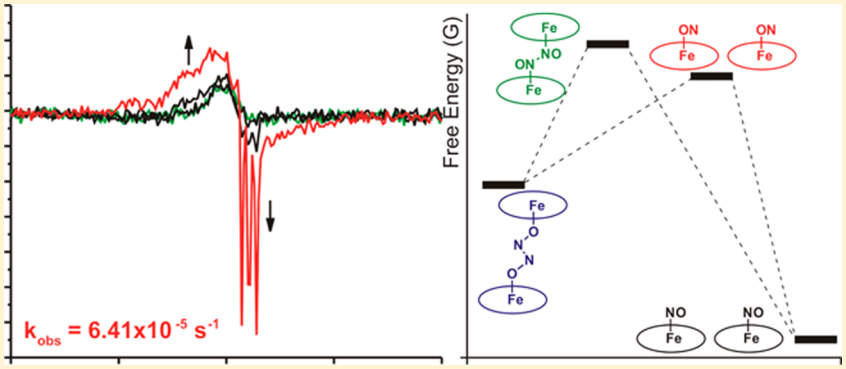

ABSTRACT: The detoxification of nitric oxide (NO) by bacterial NO reductase (NorBC) represents a paradigm of how NO can be detoxified anaerobically in cells. In order to elucidate the mechanism of this enzyme, model complexes provide a convenient means to assess potential reaction intermediates. In particular, there have been many proposed mechanisms that invoke the formation of a hyponitrite bridge between the heme b_3 and nonheme iron (Fe_B) centers within the NorBC active site. However, the reactivity of bridged iron hyponitrite complexes has not been investigated much in the literature. The model complex {[Fe(OEP)]$_2$(μ-N_2O_2)} offers a unique opportunity to study the electronic structure and reactivity of such a hyponitrite-bridged complex. Here we report the detailed characterization of {[Fe(OEP)]$_2$(μ-N_2O_2)} using a combination of IR, nuclear resonance vibrational spectroscopy, electron paramagnetic resonance, and magnetic circular dichroism spectroscopy along with SQUID magnetometry. These results show that the ground-state electronic structure of this complex is best described as having two intermediate-spin ($S = {}^3/_2$) iron centers that are weakly antiferromagnetically coupled across the $N_2O_2^{2-}$ bridge. The analogous complex {[Fe(PPDME)]$_2$(μ-N_2O_2)} shows overall similar properties. Finally, we report the unexpected reaction of {[Fe(OEP)]$_2$(μ-N_2O_2)} in the presence and absence of 1-methylimidizole to yield [Fe(OEP)(NO)]. Density functional theory calculations are used to rationalize why {[Fe(OEP)]$_2$(μ-N_2O_2)} cannot be formed directly by dimerization of [Fe(OEP)(NO)] and why only the reverse reaction is observed experimentally. These results thus provide insight into the general reactivity of hyponitrite-bridged iron complexes with general relevance for the N−N bond-forming step in NorBC.

INTRODUCTION

The mechanism of nitric oxide (NO) reduction to nitrous oxide (N_2O) within the diiron heme−nonheme active site of bacterial (respiratory) NO reductase (NorBC) is currently highly debated.[1−8] One likely intermediate is a bridged hyponitrite complex where $N_2O_2^{2-}$ is bound between the two ferric iron centers within the enzyme active site.[7,9,10] A proposed method of formation of this bridged hyponitrite species is via radical-type N−N bond formation between two coordinated NO ligands (see the "*Trans*" mechanism in Scheme 1, top).[7] In order to evaluate the general feasibility of this process and the structure and reactivity of such an intermediate, hyponitrite-bridged iron complexes need to be studied. However, information on corresponding model complexes in the

Special Issue: Insights into Spectroscopy and Reactivity from Electronic Structure Theory

Received: February 1, 2014
Published: June 27, 2014

   dx.doi.org/10.1021/ic5002573 | *Inorg. Chem.* 2014, 53, 6398−6414

Scheme 1. Overview of Proposed Mechanisms of NO Reduction by NorBC[1,8]

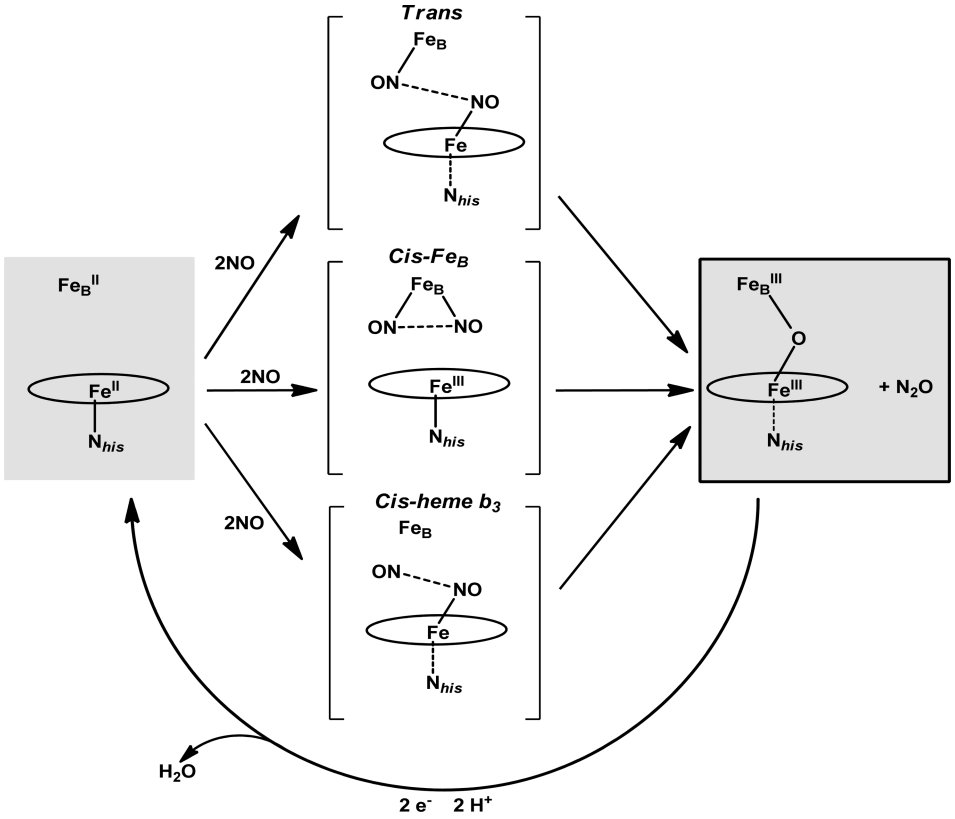

literature is sparse. Recently, the model complex {[Fe(OEP)]$_2$(μ-N_2O_2)} has been synthesized by Richter-Addo and co-workers in which two ferric octaethylporphyrin (OEP) units are bridged by the hyponitrite dianion as shown in Figure 1.[11] This complex currently represents the only structurally characterized diferric hyponitrite complex and serves as a model for the key hyponitrite-level intermediate in NorBC. Previous studies have proposed the formation of metal hyponitrite intermediates for both iron and copper complexes in the presence of excess NO.[12−14] However, these species are transient and have thus not been characterized. A handful of nonheme coordination complexes with hyponitrite ligands have been crystallized,[10,15,16] for example, in cobalt, nickel, and ruthenium complexes. In particular, Hayton and co-workers have shown N−N coupling between putative $Ni^{II}NO^-$ complexes,[16] which is mechanistically relevant for flavodiiron NO reductases (FNORs),[17,18] another class of NORs. Arikawa and co-workers observed the first case of a true radical-type N−N coupling reaction in a ruthenium−NO dimer, i.e., N−N bond formation prior to reduction of the N_2O_2 ligand.[19,20] In both of these cases, the N−N-coupled products were isolated and structurally characterized. These results are insightful, but these species do not serve as biomimetic models for the NorBC active site. The hyponitrite-bridged dimer {[Fe(OEP)]$_2$(μ-N_2O_2)} thus offers a unique opportunity to study the properties of bridged iron hyponitrite complexes with hemes and to gain insight into their biologically relevant reactivity.

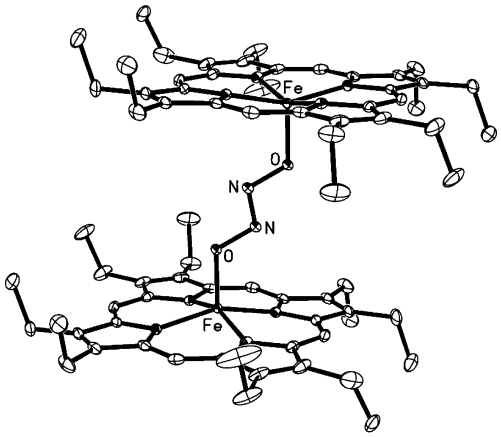

Figure 1. Molecular structure of the dinuclear ferric heme hyponitrite complex [{Fe(OEP)}$_2${μ-N_2O_2}]. Reprinted with permission from ref 11. Copyright 2009 American Chemical Society.

The electronic structure of monomeric ferrous heme nitrosyls is best described as $Fe^{II}NO$(radical).[21−23] The radical character on the bound nitrosyl can be modulated through coordination of an axial ligand trans to NO, where six-coordinate complexes with axial donor ligands impart additional radical character onto the NO moiety.[23−25] Hence, if a radical-based N−N coupling mechanism according to the "*Trans*" mechanism (see Scheme 1, top) is at all feasible, ferrous heme nitrosyls should be ideally suited to mediate this process and should spontaneously dimerize to generate N−N-coupled, bridged species, followed by hyponitrite formation. However, nothing is further from the truth because even six-coordinate ferrous heme nitrosyls have been shown to be unreactive with respect to N−N coupling and hyponitrite formation at room temperature;[1] i.e., these complexes do **not** undergo the reaction

$$2[Fe^{II}(\text{porphyrin})(NO)(L)] \not\rightarrow \{[Fe^{III}(\text{porphyrin})]_2(\mu\text{-}N_2O_2)\} \quad (1)$$

dx.doi.org/10.1021/ic5002573 | *Inorg. Chem.* 2014, 53, 6398−6414

Furthermore, these complexes do not react with NO gas at the bound nitrosyl either,[26,27] and free NO has the largest possible radical character in its uncoordinated state. Hence, the feasibility of the simple N−N radical-type coupling mechanism according to Scheme 1, top, is really in question.[1] Analysis of the electronic structure and reactivity of model complexes can thus provide further insight into alternative mechanisms of *reductive N−N coupling* that are chemically more feasible.[18] This is particularly true for reactivity studies on hyponitrite-bridged diiron complexes that model the proposed hyponitrite-bridged key intermediate of NorBC.

The model complex $\{[Fe(OEP)]_2(\mu\text{-}N_2O_2)\}$ is ideally suited to learn more about the basic properties of hyponitrite-bridged diiron complexes and their potential mechanisms of formation and decay. For this purpose, it is necessary to first develop a clear understanding of the electronic structural properties of this compound. In a previous publication, Richter-Addo and coworkers have already detailed the crystal structure of $\{[Fe(OEP)]_2(\mu\text{-}N_2O_2)\}$ (see Figure 1) and performed a vibrational characterization along with preliminary density functional theory (DFT) calculations on high-spin (S = 5), intermediate-spin (S = 3), and low-spin (S = 1) computational models of the complex.[11] Here, the DFT-calculated atomic charges reveal a high degree of anionic character on the oxygen atoms of hyponitrite. This is in agreement with the observed reactivity of this complex with HCl, where protonation of the hyponitrite bridge leads to N_2O formation along with generation of [Fe(OEP)]Cl and H_2O. Interestingly, cursory electron paramagnetic resonance (EPR) spectra of $\{[Fe(OEP)]_2(\mu\text{-}N_2O_2)\}$ recorded at 77 K show signals with g values of 5.74 and 2.03, consistent with an $S = {}^5/_2$ high-spin ferric heme. This is surprising because the two iron centers within $\{[Fe(OEP)]_2(\mu\text{-}N_2O_2)\}$ are expected to be magnetically coupled, but this contradiction could not be resolved in the previous study.

As previously reported, $\{[Fe(OEP)]_2(\mu\text{-}N_2O_2)\}$ decomposes rapidly in the presence of HCl to generate N_2O and H_2O along with [Fe(OEP)(Cl)].[11] New reactivity reported here shows that $\{[Fe(OEP)]_2(\mu\text{-}N_2O_2)\}$ also undergoes thermal decomposition to yield 2 equiv of [Fe(OEP)(NO)], the *reverse* reaction of the proposed N−N bond formation step in NO reduction according to eq 1. Given this interesting reactivity, a detailed characterization of the electronic structure and reactivity of $\{[Fe(OEP)]_2(\mu\text{-}N_2O_2)\}$ is warranted, which is presented in this paper. For this purpose, a combination of EPR, magnetic circular dichroism (MCD), nuclear resonance vibrational spectroscopy (NRVS), and SQUID magnetic susceptibility measurements has been applied. In addition, DFT calculations are absolutely critical for the interpretation of the NRVS data and, in particular, the understanding of the observed reactivity and how it relates to NOR chemistry and N−N bond formation in these enzymes. First, DFT methods are used to calculate the normal modes of the hyponitrite complexes to analyze the NRVS data and assign the spectra. Second, DFT methods assist in determining the spin state of $\{[Fe(OEP)]_2(\mu\text{-}N_2O_2)\}$ via comparison of the calculated structures and absolute energies. In this respect, we also learn how sensitive relative energies are to the choice of functional, as demonstrated here for ferric hemes, making it evident that the prediction of the spin states of transition-metal complexes based solely on DFT, i.e., in the absence of experimental data, can be challenging and misleading. Finally, the DFT calculations provide critical insight into the potential intermediates of the decomposition of $\{[Fe(OEP)]_2(\mu\text{-}N_2O_2)\}$ into 2 equiv of [Fe(OEP)(NO)]. The calculations identify two possible pathways for the reaction, either via a N-bound hyponitrite complex or via formation of isonitrosyl complexes, and the relative (free) energies of both pathways are analyzed here using different DFT methods (compared to the observed rate constants for this process). Furthermore, the DFT calculations allow us to construct a potential energy surface for this reaction and predict the relative (free) energies of reactants and products that are not experimentally available. This information can then be used to determine why the reverse reaction, the dimerization of two ferrous heme nitrosyls, is thermodynamically unfavorable and kinetically forbidden. For this detailed interpretation and understanding of the formation and decay of hyponitrite complexes, the DFT results are absolutely essential. But again, this exercise also provides a warning that DFT results should not be taken at face value and that, in order to arrive at sound conclusions, one should always consider an array of functionals and check for consistency. Results will always be dependent on the choice of the DFT method. Hence, one should never "trust" a DFT calculation, in particular in the absence of experimental data to validate the computational results.

EXPERIMENTAL AND COMPUTATIONAL PROCEDURES

Spectroscopic Measurements. The preparation and handling of air-sensitive materials was carried out under an argon atmosphere in an MBraun glovebox equipped with a circulating purifier (O_2, H_2O < 0.1 ppm). All solvents were purified by distillation under an argon atmosphere followed by three freeze−pump−thaw cycles prior to use. 1-Methylimidazole (MI) was obtained from Sigma-Aldrich and was also purified by distillation under an argon atmosphere followed by three freeze−pump−thaw cycles prior to use. The ferric high-spin complex [Fe(F_8TPP)Cl] [F_8TPP^{2-} = tetra(*o*-difluorophenyl)-porphyrin dianion] was prepared according to literature procedures.[28] This complex shows an axial EPR spectrum with g values of 6 and 2. IR spectra were obtained from KBr disks on a PerkinElmer BX spectrometer. Electronic absorption spectra were measured using an Analytical Jena Specord 600 instrument. EPR spectra were recorded on a Bruker X-band EMX spectrometer equipped with Oxford Instruments liquid nitrogen and helium cryostats. EPR spectra were typically obtained on frozen solutions using ∼20 mW microwave power and 100 kHz field modulation with the amplitude set to 1 G. SQUID susceptibility measurements were conducted on a Quantum Design MPMS-XL7 equipped with an Evercool Dewar. Samples were prepared as mixtures with either eicosane or silicon oil in a polycarbonate capsule. In a typical experiment, 5 mg of sample were used. Raw magnetic data were worked up using the program *julX*.[29] This program was also used to fit the magnetic data. The 20 mol % high-spin ferric impurity was included in the fit but only as an isotropic $S = {}^5/_2$ center with D = 0 (because the magnetic properties of this impurity are not exactly known). MCD spectra were recorded on a setup that consists of an Oxford Instruments SM4000 cryostat and a Jasco J-815 CD spectrometer. The SM4000 cryostat contains a liquid-helium-cooled superconducting magnet providing horizontal magnetic fields of 0−7 T. The J-815 spectrometer uses a gaseous nitrogen-cooled xenon lamp and a detector system consisting of two interchangeable photomultiplier tubes in the UV−visible and near-IR range. The samples were loaded into a 1.5−300 K variable-temperature insert, which offers optical access to the sample via four optical windows made from Suprasil B quartz. For MCD measurements, $\{[Fe(OEP)]_2(\mu\text{-}N_2O_2)\}$ was embedded in thin polystyrene (PS) films. The PS films were then placed between quartz plates in a custom-made sample holder. NRVS data were obtained as described previously[30] at beamline 3-ID-XOR of the Advanced Photon Source (APS) at Argonne National Laboratory. This beamline provides about 2.5 × 10^9 photons s^{-1} in ∼1 meV bandwidth (=8 cm^{-1}) at 14.4125

dx.doi.org/10.1021/ic5002573 | *Inorg. Chem.* 2014, 53, 6398−6414

keV in a 0.5 mm (vertical) × 0.5 mm (horizontal) spot. Samples were loaded into 4 × 7 × 1 mm copper NRVS cells. The final spectra represent averages of 6 scans. The program *Pheonix* was used to convert the NRVS raw data into the vibrational density of states (VDOS).[31,32]

Preparation of {[Fe(OEP)]$_2$(μ-N$_2$O$_2$)}. All reactions were performed under an atmosphere of prepurified nitrogen using standard Schlenk glassware and/or in an Innovative Technology Labmaster 100 drybox. Solutions for spectral studies were also prepared under a nitrogen atmosphere. Solvents were dried by passage through alumina (using a Pure Solv 400-5-MD system) and dearated just prior to use. The compounds [Fe(OEP)Cl],[33] [^{57}Fe(OEP)Cl],[34] and $H_2N_2O_2$,[35] (and ^{15}N-labeled $H_2{}^{15}N_2O_2$[11] and ^{18}O-labeled $H_2N_2{}^{18}O_2$) were prepared by the procedures reported for the unlabeled analogues. The [Fe(OEP)(OMe)] and [^{57}Fe(OEP)(OMe)] compounds were prepared as described for the [Fe(TPP)(OMe)] analogue reported previously.[36] Labeled sodium nitrite ($Na_2{}^{15}NO_2$, 98+%) and $^{57}Fe_2O_3$ were obtained from Cambridge Isotope Laboratories. IR spectra were recorded on a Bio-Rad FT-155 Fourier transform infrared (FT-IR) spectrometer.

{[Fe(OEP)]$_2$(μ-N$_2$O$_2$)} was prepared previously from {[Fe(OEP)]$_2$(μ-O)} in 52% yield.[11] The following method gives a better yield of the product. To a stirred CH_2Cl_2 solution (10 mL) of [Fe(OEP)(OMe)] (50 mg, 0.081 mmol) was added dropwise excess $H_2N_2O_2$ (~0.220 mmol in Et_2O). The color of the stirred solution changed from brown-red to brown-purple over a 30 min period. The solution was reduced to 2 mL in vacuo, and then hexane (15 mL) was added. The resulting solution was kept at −20 °C for 2 h. The precipitate was collected by filtration and dried in vacuo to give dark-purple microcrystals of {[Fe(OEP)]$_2$(μ-N$_2$O$_2$)} (41 mg, 0.033 mmol, 81% yield). IR (KBr, cm^{-1}): ν(N−O) = 982.

The ^{57}Fe-labeled compound {[^{57}Fe(OEP)]$_2$(μ-N$_2$O$_2$)} was generated similarly using [^{57}Fe(OEP)(OMe)]. The ^{57}Fe/^{15}N and ^{57}Fe/^{18}O doubly labeled compounds {[^{57}Fe(OEP)]$_2$(μ-^{15}N$_2$O$_2$)} and {[^{57}Fe(OEP)]$_2$(μ-N$_2{}^{18}$O$_2$)} were generated using both [^{57}Fe(OEP)(OMe)] and $H_2{}^{15}N_2O_2/H_2N_2{}^{18}O_2$. All labeled products were obtained in 75−80% yield. IR (KBr, cm^{-1}): ν(N−O) = 982 for {[^{57}Fe(OEP)]$_2$(μ-N$_2$O$_2$)} and ν(^{15}N−O) = 974 for {[^{57}Fe(OEP)]$_2$(μ-^{15}N$_2$O$_2$)}. The ν(N−O) band for {[^{57}Fe(OEP)]$_2$(μ-N$_2{}^{18}$O$_2$)} was buried under an intense porphyrin band at 957 cm^{-1}. All complexes were stored under inert gas at −34 °C until ready to use.

Preparation of {[Fe(PPDME)]$_2$(μ-N$_2$O$_2$)}. This compound was generated from reaction of the oxo dimer {[Fe(PPDME)]$_2$(μ-O)} (purchased from Midcentury Chemicals)[37] with $H_2N_2O_2$ (in Et_2O) in ~65% isolated yield. IR (KBr, cm^{-1}): ν(N−O) = 990.

Density Functional Theory (DFT). DFT calculations were performed on the full complex {[Fe(OEP)]$_2$(μ-N$_2$O$_2$)} without simplifications. Here, the geometries of the corresponding O- and N-bound species were fully optimized for both the S = 5 and 3 spin states using a number of DFT methods summarized in Table S13 in the Supporting Information (SI). These were used as implemented in *Gaussian09*. Vibrational frequency calculations performed on these optimized structures show no imaginary frequencies, indicating that true minima have been obtained (with the exception of the TPSS/TZVP structure, which has one imaginary frequency around 100*i* cm^{-1} that corresponds to a torsion of the ethyl substituents). Furthermore, similar calculations were also performed using the porphine (P^{2-}) approximation for the OEP^{2-} ligand. From these results, NRVS spectra were simulated using the program *GNRVS*. For the reaction-coordinate calculations, geometry-optimized structures were obtained with BP86/TZVP,[38−41] and single-point energies were generated using B3LYP, B3LYP*, O3LYP, and O3LYP* together with the TZVP basis set.[34,38,42−45] The program *Gaussian09* was used for geometry optimizations and frequency calculations,[46] whereas *ORCA* was used for the single-point energy calculations.[47] Similar reaction-coordinate calculations were also performed for the corresponding 1-methylimidazole (MI)-coordinated complexes in the S = 1 and 5 states. Finally, structures and single-point energies were also calculated for [Fe(OEP)(NO)] and [Fe(P)(NO)] and the corresponding MI-bound complexes for both O- and N-bound isomers in the S = $^1/_2$ spin state. These calculations were again performed using BP86/TZVP for the structures and B3LYP, B3LYP*, O3LYP, and O3LYP* for the single-point energies.

At this point, we should also comment on the electronic ground state of the proposed, five-coordinate isonitrosyl intermediate [Fe(P)(ON)]. Our calculations identified three different electronic structures for this molecule in the S = $^1/_2$ spin state. These are the Fe^{II}ON(radical) state, analogous to the ground state of ferrous heme nitrosyls with N-bound NO, and two states where the iron becomes oxidized to iron(III) and NO is reduced to the nitroxyl (NO^-) anion. These are electronic structures where (i) a singlet NO^- (S = 0) is bound to a low-spin iron(III) (S = $^1/_2$), ls-Fe^{III}ON$^-$, and (ii) a triplet NO^- (S = 1) is bound to an intermediate-spin (is) iron(III) (S = $^3/_2$), is-Fe^{III}ON$^-$, with antiferromagnetically coupled spins. Of these three electronic states, the B3LYP single-point calculations favor the is-Fe^{III}ON$^-$ state over the ls-Fe^{III}ON$^-$ state by about 30 kcal mol^{-1}. The Fe^{II}ON(radical) state is close in energy but still disfavored over the is-Fe^{III}ON$^-$ state by about 4 kcal mol^{-1}. All energies given for the five-coordinate isonitrosyl complex in this paper are therefore for the is-Fe^{III}ON$^-$ state (S = $^1/_2$). We did not further explore the potential electronic structures of the isonitrosyl complex because this is complicated by the fact that there is only very limited experimental data available for this species.[48] Hence, it is challenging to calibrate DFT calculations to obtain insight into the electronic ground state of this species. For the purpose of this study, we therefore limited ourselves to identifying the lowest-energy state of this species.

RESULTS AND ANALYSIS

1. Magnetic Properties. In an effort to more thoroughly probe the electronic structure and spin state of {[Fe(OEP)]$_2$(μ-N$_2$O$_2$)}, EPR spectroscopy at liquid helium temperature (4 K) has been employed. In the title compound, it is expected that the two iron centers are coupled via the hyponitrite bridge and, hence, this complex should be EPR-silent (in standard perpendicular-mode X-band EPR). Surprisingly, as previously reported,[11] the EPR spectrum of a frozen CH_2Cl_2 solution of a {[Fe(OEP)]$_2$(μ-N$_2$O$_2$)} sample does show signals consistent with an S = $^5/_2$ high-spin complex (see Figure 2). However, spin quantification against an S = $^5/_2$ standard of known concentration shows that this signal corresponds to a minor component of the {[Fe(OEP)]$_2$(μ-N$_2$O$_2$)} sample (~20 mol % impurity = ~10 mol % in iron centers; Figure S1 in the SI). It is therefore more accurate to assign {[Fe(OEP)]$_2$(μ-N$_2$O$_2$)} at 4

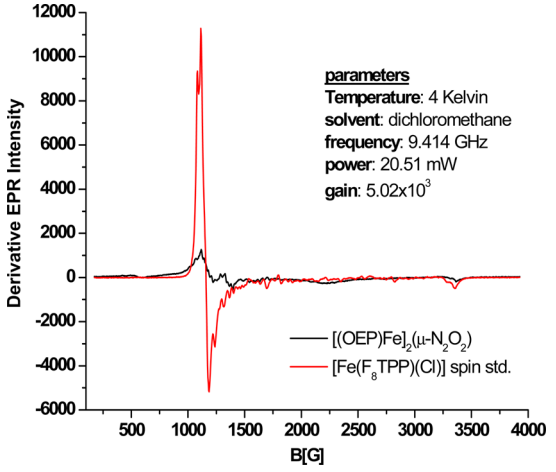

Figure 2. EPR spectrum of {[Fe(OEP)]$_2$(μ-N$_2$O$_2$)} versus the S = $^5/_2$ spin standard [Fe(F_8TPP)Cl] recorded at 4 K. The solutions are 3 mM in iron centers.

dx.doi.org/10.1021/ic5002573 | Inorg. Chem. 2014, 53, 6398−6414

K as EPR-silent, displaying either ferromagnetic (integer spin) or antiferromagnetic ($S = 0$) coupling across the hyponitrite bridge. The presence of this minor $S = {}^5/_2$ component is consistent across multiple preparations of {[Fe(OEP)]$_2$(μ-N_2O_2)}, obtained from either {[Fe(OEP)]$_2$(μ-O)} (ref 11) or [Fe(OEP)(OMe)] (this work). Because the target complex is formed directly from the reaction of the porphyrin precursor with excess hyponitrous acid, which decomposes readily into N_2O and water, we believe that the impurity is very likely [Fe(OEP)(OH)], formed from the water generated from $H_2N_2O_2$ decomposition in an overall acidic reaction mixture. This is the only likely monomeric high-spin ferric product that could form under our reaction conditions (see the Experimental Section). In this regard, please note that ferric porphyrin hydroxo complexes show axial EPR spectra with g values of ~6 and 2, as reported previously,[49] in close agreement with the spectrum obtained here for the ferric impurity. Unfortunately, despite much effort, the presence of this impurity cannot be avoided, and this has to be accounted for in our data interpretations. Because the impurity only corresponds to about 10 mol % in iron centers, this should only have a relatively minor effect on the following spectroscopic studies. EPR spectra obtained on bulk solid samples of {[Fe(OEP)]$_2$(μ-N_2O_2)} at 4 K show highly distorted signals indicative of intermolecular spin coupling in the solid state (Figure S2 in the SI).[50]

Because {[Fe(OEP)]$_2$(μ-N_2O_2)} is EPR-silent, SQUID susceptibility measurements were employed in an effort to determine the molecular spin state of this complex. As shown in Figure 3, the effective magnetic moment of {[Fe(OEP)]$_2$(μ-N_2O_2)} is essentially constant above 100 K, indicating that the iron(III) centers in the hyponitrite-bridged dimer are only weakly magnetically coupled. This makes intuitive sense because the iron centers are separated by a four-atom bridge. In addition, the shape of the $\chi_M T$ versus T data clearly indicates antiferromagnetic coupling between the iron(III) centers, which is nicely illustrated in the J-space exploration in Figure S3 in the SI. A fit of the $\chi_M T$ versus T data with *julX* using a standard exchange Hamiltonian, $H = -2J \cdot S_1 \cdot S_2$, is only possible if the iron centers are in an intermediate, $S = {}^3/_2$ state which is a surprising result. The best fit gives an exchange coupling constant, J, of -2.5 cm^{-1}. The fit can be further improved if zero-field splitting is considered, as shown in Figure 3, top. In this case, the best fit is obtained with $J = -1.33$ cm^{-1} and $D = 20$ cm^{-1}, with again $S = {}^3/_2$ iron(III) centers. The residual deviations in the fit are likely due to the 20 mol % impurity (per dimer) of a mononuclear $S = {}^5/_2$ complex, as is evident and quantified by EPR spectroscopy. Figure 3, bottom, shows the effective magnetic moment (in Bohr magnetons) plotted against the temperature, including the two fits mentioned above. The effective magnetic moment (μ_{eff}) is 5.53 μ_{BM} at 250 K per dimer.

In support of the observed very weak exchange coupling between the iron(III) centers, low-temperature (<50 K) VTVH MCD spectra of {[Fe(OEP)]$_2$(μ-N_2O_2)} embedded in a polystyrene (PS) matrix show both temperature- and field-dependent saturation, as shown in Figure 4. This observation is in accordance with the MCD C-term intensity resulting from a paramagnetic complex and could be explained with either ferromagnetic or very weak antiferromagnetic coupling between the two iron centers.[51] In the latter case, a *strongly* antiferromagnetically coupled spin state would be expected to lead to an isolated diamagnetic ground state and, hence, a lack

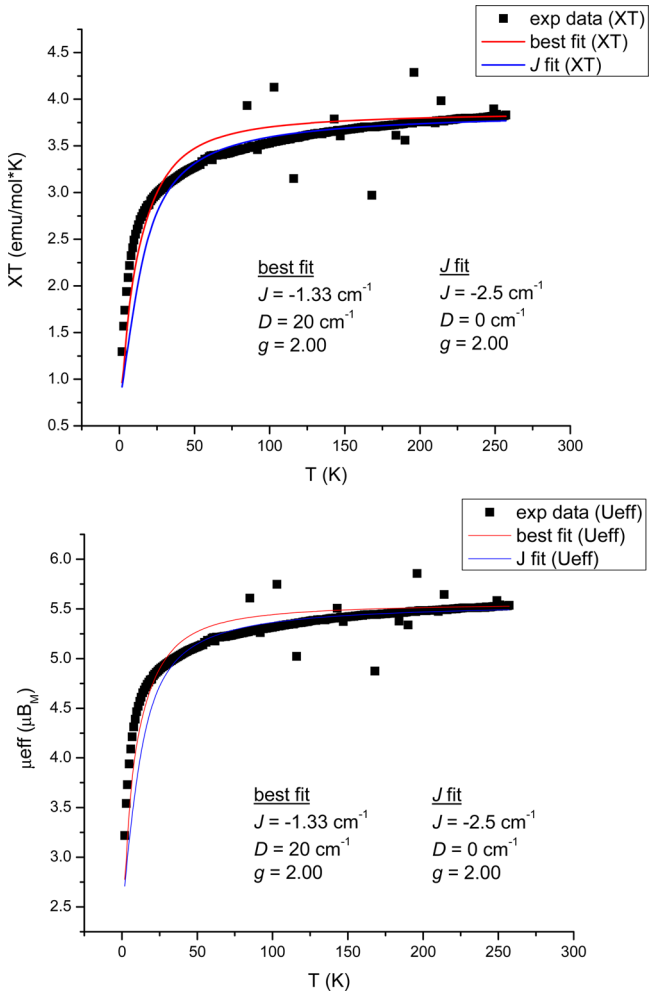

Figure 3. SQUID susceptibility data for {[Fe(OEP)]$_2$(μ-N_2O_2)}. Plot of $\chi_M T$ versus temperature, T (top), and μ_{eff} versus T (bottom). Fits of the data using *julX* are also included. Experimental data are not corrected for the observed ferric impurity (see the text).

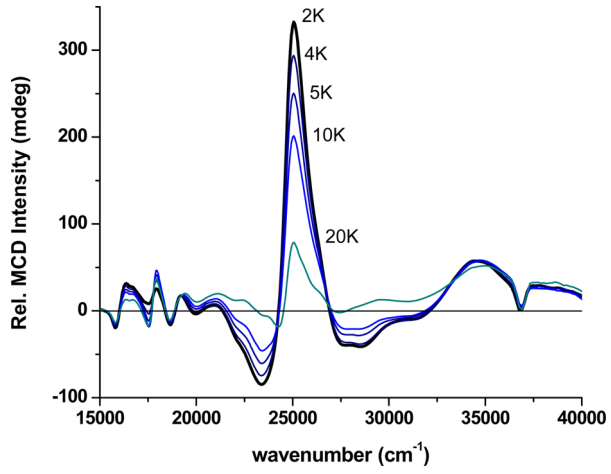

Figure 4. MCD spectra of {[Fe(OEP)]$_2$(μ-N_2O_2)} recorded at 7 T across multiple temperatures as indicated.

of C-term intensity at low temperature (cf. Figure S3 in the SI). Therefore, the MCD intensity would not show temperature-dependent saturation, which is clearly not the case. The average MCD spectra of {[Fe(OEP)]$_2$(μ-N_2O_2)} taken at 2 K between

dx.doi.org/10.1021/ic5002573 | Inorg. Chem. 2014, 53, 6398−6414

1 and 7 T are shown in Figure S6 in the SI. Magnetization plots generated from the $\{[Fe(OEP)]_2(\mu\text{-}N_2O_2)\}$ MCD data show, as expected, a high degree of nesting (see Figure S5 in the SI) due to the expected, strong zero-field splitting in a d^5, $S = {}^3/_2$ electronic state (estimated to be about 20 cm^{-1} from the magnetic data; see above). Because of the presence of the ferric impurity (see above), fitting of the MCD data to determine the total spin is nontrivial and was not attempted. However, as mentioned above, the MCD results directly support the results from the SQUID measurements.

2. Vibrational Spectroscopy. Vibrational data were obtained using both FT-IR and NRVS[52,53] spectroscopy to gain more insight into the nature of the hyponitrite bridge and to expand on the magnetic data presented above. Here, vibrational assignments are significant because the vibrational energies provide insight into the bond strengths and energies within the hyponitrite unit. The antisymmetric N−O stretching mode of $\{[Fe(OEP)]_2(\mu\text{-}N_2O_2)\}$ has been previously assigned to an IR band at 982 cm^{-1} based on ^{15}N labeling of the hyponitrite bridge.[11] In addition, a weak isotope-sensitive band is present at 436 cm^{-1} in the IR spectrum, as shown in Figure S7 in the SI. This feature is sensitive to both ^{15}N and ^{18}O labeling and is therefore associated with the bound hyponitrite ligand. Because the FT-IR features associated with the Fe−O−N−N−O−Fe unit are relatively weak and difficult to identify, NRVS measurements were employed in an attempt to further elucidate the vibrational structure of $\{[Fe(OEP)]_2(\mu\text{-}N_2O_2)\}$. As shown in Figure 5, the NRVS data indeed identify an additional single isotope-sensitive band at 322 cm^{-1} that shifts to 310 cm^{-1} upon $^{15}N^{18}O$ labeling. The assignments of these features are further discussed in conjuncture with DFT calculations; see the following section 3.

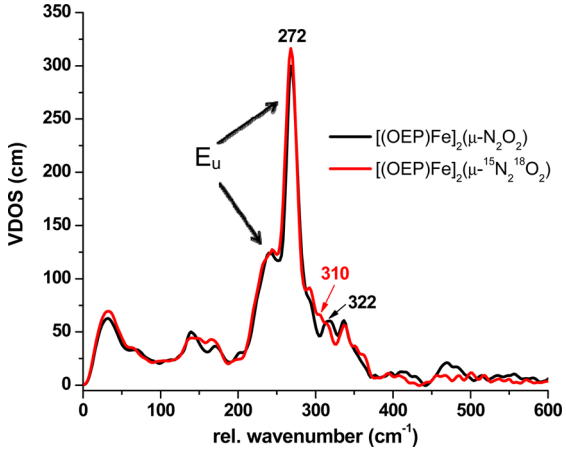

Figure 5. NRVS spectra of $\{[Fe(OEP)]_2(\mu\text{-}N_2O_2)\}$ and of the corresponding $^{15}N_2{}^{18}O_2$-isotope-labeled complex.

Considering that NRVS intensity is directly correlated with ^{57}Fe motion within a given vibrational mode,[54] it is surprising that only one isotope-sensitive feature can be identified in the NRVS data of $\{[Fe(OEP)]_2(\mu\text{-}N_2O_2)\}$ and that the intensity of this feature is relatively weak. One would expect that the symmetric and antisymmetric Fe−O stretching vibrations of the hyponitrite bridge should show a distinct amount of iron motion and, hence, NRVS intensity.[34] Correspondingly, heme nitrosyls show Fe−N−O stretching and bending vibrations that are very intense in NRVS.[52] This aspect is further discussed in the next section.

3. DFT Calculations. DFT calculations were employed (a) to aid in the assignment of the vibrational features of $\{[Fe(OEP)]_2(\mu\text{-}N_2O_2)\}$ and to investigate the lack of intense NRVS features for this complex and, most importantly, (b) to obtain insight into the reactivity of this interesting species.

Calculated Structures. In order to test whether the structural parameters would provide further insight into the spin state of $\{[Fe(OEP)]_2(\mu\text{-}N_2O_2)\}$, we fully optimized the structure of this complex, including the full OEP^{2-} ligand, with both BP86/TZVP and B3LYP/6-31G* for both the $S = 3$ and 5 total spin states, i.e., with the iron centers either in an intermediate-spin ($S = {}^3/_2$) or high-spin ($S = {}^5/_2$) state. Experimentally, it was shown that the iron centers in the hyponitrite-bridged dimer are weakly antiferromagnetically coupled as described above. However, optimizing the corresponding broken-symmetry states ($S = 0$) for the $S = {}^3/_2$ and ${}^5/_2$ cases turned out to be essentially impossible. Nevertheless, because the exchange coupling is very weak ($J = -1$ to -2 cm^{-1}; see above), the geometric, vibrational, and even energetic differences that could be caused by this coupling are, in fact, very small. Hence, we can use the corresponding ferromagnetically coupled systems with $S = 3$ and 5 total spins for the DFT calculations without any loss in accuracy.

The resulting geometric parameters for the $Fe{-}N_2O_2{-}Fe$ bridge are summarized in Table 1. As is evident from Table 1, the B3LYP calculation on the $S = 3$ state reproduces the structural parameters of $\{[Fe(OEP)]_2(\mu\text{-}N_2O_2)\}$ extremely well, providing further support for the idea that the iron centers are in an intermediate-spin state ($S = {}^3/_2$) in the dimer. The Fe−O bond is predicted at 1.90 and 1.87 Å for the $S = 3$ and 5 models, respectively, which compares well to 1.89 Å observed in the crystal structure. Furthermore, O−N distances and Fe−O−N angles are obtained at 1.36 and 118° for both the

Table 1. Comparison of DFT-Predicted (Fully Optimized) and Experimental Geometric Properties [Å and deg] of the Hyponitrite Bridge in $\{[Fe(OEP)]_2(\mu\text{-}N_2O_2)\}$ (Using the Full OEP^{2-} Ligand in the Calculations) and $\{[Fe(P)]_2(\mu\text{-}N_2O_2)\}$ (Using the Porphine (P^{2-}) Approximation)

	$\{[Fe(OEP)]_2(\mu\text{-}N_2O_2)\}$					$\{[Fe(P)]_2(\mu\text{-}N_2O_2)\}$	
	BP86/TZVP		B3LYP/6-31G*			BP86/TZVP	
	$S = 3$	$S = 5$	$S = 3$	$S = 5$	crystal structure	$S = 3$	$S = 5$
Fe−O	1.95	1.91	1.90	1.87	1.889(2)	1.94	1.90
N−O	1.35	1.35	1.36	1.36	1.375(2)	1.34	1.35
N−N	1.28	1.27	1.25	1.25	1.250(3)	1.28	1.27
Fe---Fe	6.90	6.82	6.70	6.65	6.69	6.89	6.83
Fe−O−N	123	123	118	118	118.6(1)	124	125
O−N−N	110	109	110	109	108.5(2)	110	109

dx.doi.org/10.1021/ic5002573 | Inorg. Chem. 2014, 53, 6398−6414

S = 3 and 5 models, respectively, compared to 1.38 Å and 118.6° in the crystal structure. Finally, the Fe---Fe distance in the dimer is predicted at 6.70 and 6.65 Å for the S = 3 and 5 models, respectively, close to the experimental value of 6.69 Å. Additional geometric parameters are listed in Table 1. We note that the experimental crystal structure of $\{[Fe(OEP)]_2(\mu\text{-}N_2O_2)\}$ contains CH_2Cl_2 solvates that closely flank the hyponitrite bridge; we do not, however, have any evidence at this time that the presence of the solvates influences the hyponitrite bond parameters.

In contrast, the BP86 results for the complete hyponitrite-bridged dimer (although clearly within the acceptable range for DFT structures of large molecules) are of inferior quality and do not allow one to draw conclusions about the spin state of the molecule. We also tested whether the popular porphine approximation would give comparable structures. As shown in Table 1 (right), the BP86/TZVP calculations on $\{[Fe(P)]_2(\mu\text{-}N_2O_2)\}$ for both S = 3 and 5 spin states indeed give identical structures for the Fe–N_2O_2–Fe unit compared to the full molecule. Hence, it is valid to use the porphine approximation to investigate the reactivity of the hyponitrite bridge (see below). This strategy is favorable because it saves a tremendous amount of computational time. Not only does it reduce the number of atoms in the dimer dramatically, but the ethyl substituents in OEP^{2-} are also very flexible and sometimes cause difficulty during geometry optimizations.

Finally, we also tested the more "modern" functionals OLYP, O3LYP, TPSS, TPSSH, and PBE1PBE to examine whether any of these methods would reproduce the structural properties of $\{[Fe(OEP)]_2(\mu\text{-}N_2O_2)\}$. For this purpose, the complete molecule was again used, i.e., utilizing the complete OEP^{2-} ligand, and the structures for the S = 3 spin state were fully optimized with these different methods. These results, summarized in Table S13 in the SI, show no further improvement over the B3LYP and BP86 calculations. On the contrary, the computed structures with PBE1PBE, O3LYP, and TPSSH show quite severe distortions where the two hemes are no longer coplanar, and for PBE1PBE and O3LYP, the planarity of the Fe–N_2O_2–Fe unit is also lost. These structures are not in agreement with experiment and document how difficult (and unreliable) it can be to predict the structures of large molecules from simple DFT calculations in the absence of experimental data to validate the structures.

Calculated Vibrational Properties. Frequency calculations on the full complex $\{[Fe(OEP)]_2(\mu\text{-}N_2O_2)\}$ were first employed to analyze the NRVS spectra of this complex. However, the agreement obtained between the DFT-calculated spectra and the experimental data is quite poor, as is evident from Figures S25 and S26 in the SI. Curiously, hybrid functionals give a particularly bad agreement with experiment, despite the fact that the geometry of the complex is well reproduced by these methods (in particular, with B3LYP). The best agreement is, in fact, obtained with BP86, as shown in Figure S25 in the SI, but the overall deviations from experiment are still large. As previously reported, the underlying reason for this deviation is a strong coupling between the low-energy porphyrin core vibrations and bending and torsional modes of the peripheral ethyl substituents of the OEP^{2-} ligand,[34] which are not reproduced well by any DFT method. This particularly affects the E_u-symmetric Fe–N_{pyr} (pyr = pyrrole) stretching mode, which is usually the most intense feature in the NRVS spectra of iron porphyrins. In the case of $\{[Fe(OEP)]_2(\mu\text{-}N_2O_2)\}$, this coupling leads to a splitting of the E_u vibration

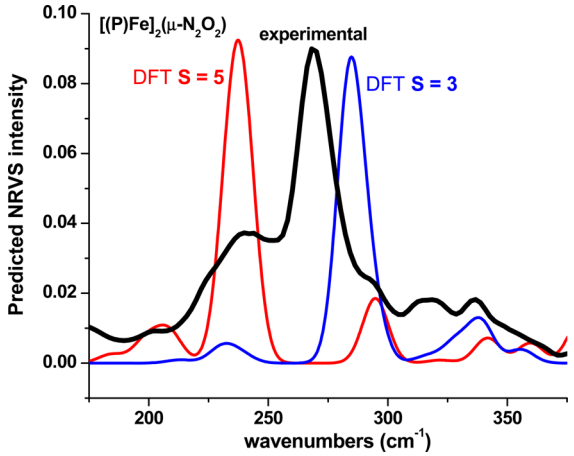

Figure 6. DFT-predicted versus experimental NRVS data showing the shift in the porphyrin-based E_u-symmetric Fe–N_{pyr} stretching mode upon a change in the spin state. Spectra predicted with the porphine approximation (BP86/TZVP) show single narrow E_u features of high intensity. In comparison, the E_u modes in OEP^{2-} complexes are generally broadened and oftentimes split because of intense couplings with bending modes and torsions of the peripheral ethyl substituents. In order to account for this difference, the NRVS intensity of the calculated spectra has been scaled down by 50% for a better comparison with the experimental data.

Table 2. Comparison of DFT-Predicted (BP86/TZVP) and Experimental Vibrational Properties [cm^{-1}] for $\{[Fe(OEP)]_2(\mu\text{-}N_2O_2)\}$

	$\{[Fe(P)]_2(\mu\text{-}N_2O_2)\}$		$\{[Fe(OEP)]_2(\mu\text{-}N_2O_2)\}$
	DFT: S = 3[a]	DFT: S = 5[a]	experimental
ν(N–N)	1230 (0.001)	1279 (0.001)	
$\nu(N-O)_{as}$	1025 (0.000)	1011 (0.000)	982
$\nu(N-O)_s$	967 (0.002)	964 (0.001)	
$\delta(O-N-N)_s$	703 (0.01)	742 (0.02)	
$\delta(O-N-N)_{as}$ + $\nu(Fe-O)_{as}$	509 (0.073) [3%]	526 (0.117) [4%]	436 (?)
$\nu(Fe-O)_{as}$ + $\delta(Fe-O-N)_{as}$ + porphyrin(oop)	339 (0.318) [14%]	342 (0.190) [7%]	436 (?)
$\gamma(O-N-N-O)_s$	314 (0.015)	323 (0.000)	
$\nu(Fe-O)_s$ + E_u(porphyrin)	293 (0.431) [19%]	295 (0.494) [18%]	322
E_u(porphyrin)	~285 (2.27) [100%]	~234 (2.80) [100%]	272/(241)

[a]In round brackets: DFT-calculated NRVS (VDOS) intensities. In square brackets: percent intensity compared to the E_u porphyrin mode. s = symmetric and as = antisymmetric.

into two components observed at 272 and 241 cm^{-1} (see Figures 5 and 6 and Table 2) and a broadening of these NRVS signals. This effect can be quite extreme: for example, recent work by Sage and co-workers has shown that, in the case of the simple chloro complex [Fe(OEP)Cl)], the E_u-symmetric Fe–N_{pyr} stretching mode is observed as an extremely broad, featureless band that ranges from 200 to 300 cm^{-1}.[55] In contrast, the NRVS data for [Fe(PPIX)(Cl)] and [Fe(P)(Cl)] ($PPIX^{2-}$ = protoporphyrin IX dianion; P^{2-} = porphine dianion) show single, very intense NRVS signals for this mode.[55]

Because of these complications and the overall poor agreement between the experimental and calculated NRVS data for $\{[Fe(OEP)]_2(\mu\text{-}N_2O_2)\}$, it seems advantageous to

dx.doi.org/10.1021/ic5002573 | Inorg. Chem. 2014, 53, 6398–6414

focus the vibrational analysis on the calculated spectra obtained with the porphine approximation, which are not affected by the challenges DFT faces in describing the vibrational couplings between the porphyrin core and periphery modes accurately. The large deviations in the calculated energies of the porphyrin core vibrations in $\{[Fe(OEP)]_2(\mu\text{-}N_2O_2)\}$ also affect the energies and intensities of the hyponitrite vibrations at low energy. Hence, for analysis of the vibrations of the Fe−N_2O_2−Fe bridge, it is therefore also advantageous to use the porphine approximation. Figure 6 shows a comparison of the experimental NRVS data for $\{[Fe(OEP)]_2(\mu\text{-}N_2O_2)\}$ and the BP86/TZVP-calculated spectra for $\{[Fe(P)]_2(\mu\text{-}N_2O_2)\}$ for both the S = 3 and 5 spin states. The calculations predict a total of eight vibrational modes with significant Fe−O−N−N−O−Fe character between ∼300 and 1300 cm^{-1}, as shown in Table 2. For the S = 3 model, both the symmetric and antisymmetric N−O stretching modes predicted at 967 and 1025 cm^{-1}, respectively, are within 50 cm^{-1} of the experimentally observed 982 cm^{-1} feature. Because this mode is observed in the FT-IR spectrum, it is most likely the antisymmetric stretch, as previously stated, due to the IR-forbidden nature of the corresponding symmetric mode.

To lower energy, the DFT calculations predict the symmetric and antisymmetric O−N−N bending modes at 703 and 509 cm^{-1}, followed by the antisymmetric Fe−O−N bend at 339 cm^{-1} (all for S = 3). Interestingly, the latter two modes at 509 and 339 cm^{-1} also have significant contributions of the antisymmetric Fe−O stretch. But surprisingly, the calculated NRVS intensities for these modes are very small. The assignment of the $^{15}N_2{}^{18}O_2$-isotope-sensitive FT-IR feature at 436 cm^{-1} is unclear. In principle, this mode could be assigned to either the 509 or 339 cm^{-1} vibration, but in both cases, the deviation from the experimental data would be very significant. Both of these modes have the appropriate symmetry to be IR-active. It is possible that the energies of these bending modes are affected by the presence of the ethyl substituents in the OEP^{2-} ligand, but this remains speculative. To lower energy of these features, the calculations predict the symmetric O−N−N−O out-of-plane bending mode at 314 cm^{-1}, and finally the symmetric Fe−O stretch at 293 cm^{-1} (all for S = 3). The latter mode has the largest predicted NRVS intensity of all vibrations associated with the Fe−N_2O_2−Fe unit and is therefore assigned to the experimentally observed NRVS feature at 322 cm^{-1}.

It is interesting to note from Table 2 that the vibrations of the Fe−N_2O_2−Fe unit in $\{[Fe(OEP)]_2(\mu\text{-}N_2O_2)\}$ are all quite weak in NRVS, which was unexpected. In comparison, the Fe−N−O stretching and bending vibrations in heme nitrosyls reach NRVS intensities of about 50% of the E_u-symmetric Fe−N_{pyr} (pyr = pyrrole) stretching mode of the heme, which is usually the dominating feature in iron porphyrin NRVS data as discussed above.[21] Exceptions are six-coordinate ferrous heme nitrosyls as discussed in ref 24. The reasons that the vibrations of the Fe−N_2O_2−Fe unit in $\{[Fe(OEP)]_2(\mu\text{-}N_2O_2)\}$ only give weak signals in NRVS are two-fold. First, in the dimeric structure of the complex, the symmetric Fe−O stretching motion can be accomplished by *rotation* of the bridging $N_2O_2{}^{2-}$ ligand, and the antisymmetric Fe−O stretch corresponds to a *translation* of the $N_2O_2{}^{2-}$ unit. In this way, the displacements of the iron centers are reduced. Representative arrow diagrams of the calculated vibrations at 509 and 293 cm^{-1} are shown in Figure 7 to illustrate this point. Interestingly, a similar behavior is observed in diazene-bridged dicopper and diiron complexes,[56−58] where most of the displacement in the metal

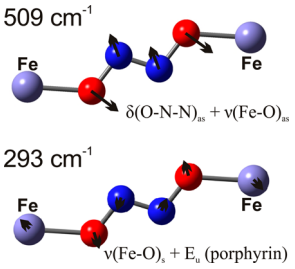

Figure 7. Arrow diagrams of the normal modes at 509 and 293 cm^{-1} (see Table 2), calculated for $\{[Fe(P)]_2(\mu\text{-}N_2O_2)\}$ (S = 3) with BP86/TZVP. The figure shows the Fe−N_2O_2−Fe core of the complexes, whereas the hemes are omitted for clarity.

diazene stretching modes is located on the bridging diazene ligand.[59] Interestingly, it was shown in these cases that the metal displacements can be increased if the effective mass of the diazene ligand is increased, for example, by methyl substitution or via hydrogen bonding. Second, the Fe−O bonds in the hyponitrite complex are weaker than the Fe−NO bonds in heme nitrosyls, which also causes a reduction in the amount of iron displacement. Despite these problems, the NRVS data of $\{[Fe(OEP)]_2(\mu\text{-}N_2O_2)\}$ allow for the identification of the symmetric Fe−O stretch, which is assigned here for the first time for a bridged hyponitrite complex. This is a key mode that characterizes the strength of the Fe−O bond in these types of complexes.

Vibrational data were also calculated for the high-spin S = 5 $\{[Fe(P)]_2(\mu\text{-}N_2O_2)\}$ model, where both iron centers are in the high-spin ($S = {}^5/_2$) state. As shown in Table 2, the calculated vibrational energies for the Fe−N_2O_2−Fe unit in this complex are generally in close agreement with those of the intermediate-spin S = 3 model. Hence, on the basis of these results alone, no distinction between the S = 3 and 5 states can be made.

In addition to vibrational features associated specifically with the Fe−O−N−N−O−Fe moiety, NRVS allows for accurate identification of the porphyrin in-plane Fe−N_{pyr} (pyr = pyrrole) stretching mode of E_u symmetry in heme-containing samples.[24] As shown in Table 2, this mode is predicted to be highly sensitive to the total spin of the complex. Here, the porphine E_u feature is predicted at 234 and 285 cm^{-1} for the S = 5 and 3 $\{[Fe(P)]_2(\mu\text{-}N_2O_2)\}$ models, respectively, as shown in Figure 6 (calculated with BP86/TZVP). The position of the E_u mode supports the $S = {}^3/_2$ spin state of the $[Fe(OEP)]^+$ centers. Inclusion of the complete OEP^{2-} ligand in the DFT model (BP86/TZVP) leads to a splitting of the E_u mode into major (higher energy) and minor (lower energy) components because of vibrational couplings with the peripheral ethyl substituents in OEP^{2-} compared to the $porphine^{2-}$ complex as discussed above (see Figures 6 and S25 in the SI). Taken together, the results on the $porphine^{2-}$ models are consistent with an intermediate spin ($S = {}^3/_2$) of the iron centers in the $\{[Fe(OEP)]_2(\mu\text{-}N_2O_2)\}$ dimer, but do not exclude the possibility that the iron centers could be high spin ($S = {}^5/_2$).

4. Reactivity and Decomposition of $\{[Fe(OEP)]_2(\mu\text{-}N_2O_2)\}$. We showed previously that the hyponitrite-bridged dimer $\{[Fe(OEP)]_2(\mu\text{-}N_2O_2)\}$ reacts with the acid HCl to generate N_2O. Curiously, we also found that this product is obtained by thermal decomposition of the hyponitrite-bridged dimer in a KBr pellet. For example, the IR spectra of a freshly prepared KBr pellet of $\{[Fe(OEP)]_2(\mu\text{-}N_2O_2)\}$ and that of the same sample after placement in the IR spectrometer chamber

dx.doi.org/10.1021/ic5002573 | Inorg. Chem. 2014, 53, 6398−6414

for 3 h are shown in Figure S8, top, in the SI. The $\nu(N-O)_{as}$ band of the hyponitrite moiety at 982 cm^{-1} decreases, and two new bands at 2218 and 881 cm^{-1} appear. The latter band is due to $\{[Fe(OEP)]_2(\mu\text{-}O)\}$. The band at 2218 cm^{-1} shifts to 2150 cm^{-1} when $\{[^{57}Fe(OEP)]_2(\mu\text{-}^{15}N_2O_2)\}$ is used and to 2212 cm^{-1} when $\{[^{57}Fe(OEP)]_2(\mu\text{-}N_2{}^{18}O_2)\}$ is used; these bands are similar to those reported by Radziszewski et al. for $N_2{}^{18}O$ (2217 cm^{-1}) and $^{15}N_2O$ (2154 cm^{-1}).[60]

Interestingly, we also discovered another, and surprising, pathway of decomposition of the $\{[Fe(OEP)]_2(\mu\text{-}N_2O_2)\}$ complex in solution. This complex is stable in solution during its preparation and in the presence of the reagent $H_2N_2O_2$ used in its synthesis. However, we first noticed the generation of small amounts of the known five-coordinate complex [Fe(OEP)(NO)] in our crystallization attempts of $\{[Fe(OEP)]_2(\mu\text{-}N_2O_2)\}$ in the absence of excess $H_2N_2O_2$. Notably, this decomposition of $\{[Fe(OEP)]_2(\mu\text{-}N_2O_2)\}$ to [Fe(OEP)(NO)] also occurs in the crystalline phase. For example, we observed that a crystalline sample of the hyponitrite species under dinitrogen decomposes quantitatively to [Fe(OEP)(NO)] over a 3 week period at room temperature, as judged by IR spectroscopy (Figure S8, bottom, in the SI).

Importantly, *this hyponitrite-to-nitrosyl reaction is in essence the reverse of that proposed during NO reduction in the active site of NorBC*, where two Fe–NO units are proposed to conduct a radical-type N–N coupling to yield a hyponitrite-bridged dimer:[7] $2[Fe(OEP)(NO)] \rightleftarrows \{[Fe(OEP)]_2(\mu\text{-}N_2O_2)\}$. However, ferrous heme nitrosyls are stable in solution and do not spontaneously dimerize. It is for this very reason that $\{[Fe(OEP)]_2(\mu\text{-}N_2O_2)\}$ could only be obtained from the preformed $N_2O_2{}^{2-}$ moiety (as hyponitrous acid). This relates back to the extraordinary stability of the Fe–NO bond in ferrous heme nitrosyls.[21] The synthetic model complex $\{[Fe(OEP)]_2(\mu\text{-}N_2O_2)\}$ thus offers the unique opportunity to study the reactivity and electronic structure of the diiron hyponitrite moiety outside of a reactive protein environment. In particular, elucidation of the mechanism (e.g., Scheme 2) of dissociation of the complex can shed light on the proposed radical N–N coupling step of the nitrosyl moieties within NorBC. *Because the N–N coupling reaction via dimerization of two ferrous heme nitrosyls cannot directly be studied, we can obtain insight into the energetics of this reaction but studying the reverse (back)reaction* (see Scheme 2).

In order to experimentally probe the thermal decomposition of $\{[Fe(OEP)]_2(\mu\text{-}N_2O_2)\}$ to [Fe(OEP)(NO)] in solution, UV–visible absorption and EPR spectroscopy were employed. EPR spectroscopy shows clear decomposition to [Fe(OEP)(NO)] as the final product; spectra recorded on thermally annealed samples of $\{[Fe(OEP)]_2(\mu\text{-}N_2O_2)\}$ in toluene show

Scheme 2. Potential Decomposition Pathways of $\{[Fe(OEP)]_2(\mu\text{-}N_2O_2)\}$

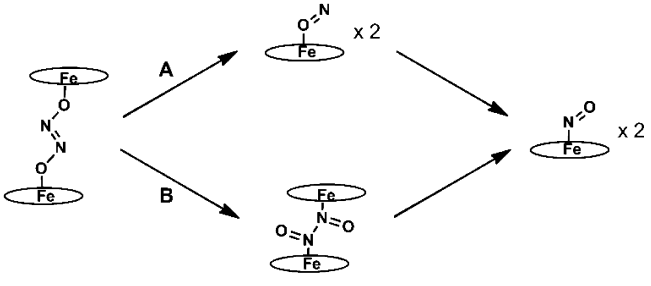

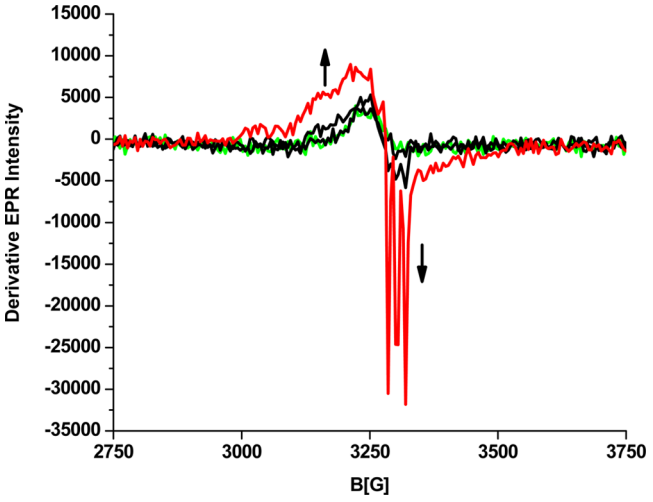

Figure 8. EPR spectra recorded during thermal annealing of $\{[Fe(OEP)]_2(\mu\text{-}N_2O_2)\}$ (1.5 mM) in CH_2Cl_2. Initial spectrum: green (t = 0), followed by spectra at t = 30, 45, and 90 min (final spectrum: red). The final product spectrum is indicative of [Fe(OEP)(NO)], showing the typical three-line hyperfine splitting of the lowest g value (see the text).[61]

slow decomposition to reveal a rhombic $S = {}^1/_2$ species with a clear three-line hyperfine splitting on g_{min} (see Figure 8). These data are consistent with the formation of a ferrous heme nitrosyl, where coupling of the nuclear spin (I = 1) of ^{14}N of NO with the electron spin ($S = {}^1/_2$) leads to a characteristic three-line hyperfine splitting.[21,61] In addition, absorption measurements, shown in Figure 9, performed at 30 °C in

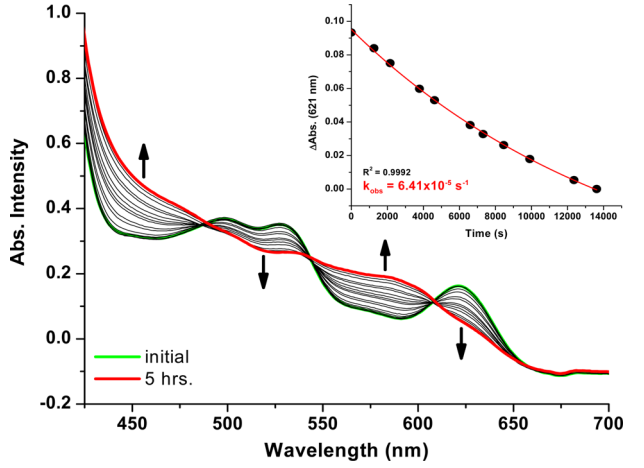

Figure 9. Absorption spectra following thermal decomposition of $\{[Fe(OEP)]_2(\mu\text{-}N_2O_2)\}$ in CH_2Cl_2 at 30 °C over the course of 5 h. Inset: difference spectra between the data obtained at a given point in time minus the last data set collected. A single-exponential fit of the absorption data is also included.

CH_2Cl_2 show a clean isosbestic conversion of the 620 nm Q band of $\{[Fe(OEP)]_2(\mu\text{-}N_2O_2)\}$ into a new species with broad absorption features between 565 and 595 nm; consistent with the formation of [Fe(OEP)(NO)].[62] The observed rate constant for this transformation was measured as 6.4×10^{-5} s^{-1} under the given conditions (see the inset in Figure 9). The slow rate constant corresponds to a kinetic barrier of roughly 20 kcal mol^{-1} from simple transition state theory [$k = (RT/Nh)e^{-\Delta G/RT}$] and is in general agreement with the DFT results,

dx.doi.org/10.1021/ic5002573 | Inorg. Chem. 2014, 53, 6398–6414

which predict high-energy intermediates in the decomposition pathway (see below). Both absorption and EPR spectroscopy are thus in agreement with the IR spectroscopic results and clearly show formation of the five-coordinate [Fe(OEP)(NO)] complex as the reaction product.

In the presence of 1-methylimidazole (MI), used as a model for histidine (His) as the proximal ligand in many heme proteins, a 1 mM toluene solution of $\{[Fe(OEP)]_2(\mu\text{-}N_2O_2)\}$ decomposes to yield [Fe(OEP)(NO)] at noticeably faster rates than those in the absence of the axial imidazole base (Scheme 3). As monitored by EPR spectroscopy at 77 K, full conversion

Scheme 3. Decomposition of $\{[Fe(OEP)]_2(\mu\text{-}N_2O_2)$ in the Presence of 1-Methylimidazole (MI)[a]

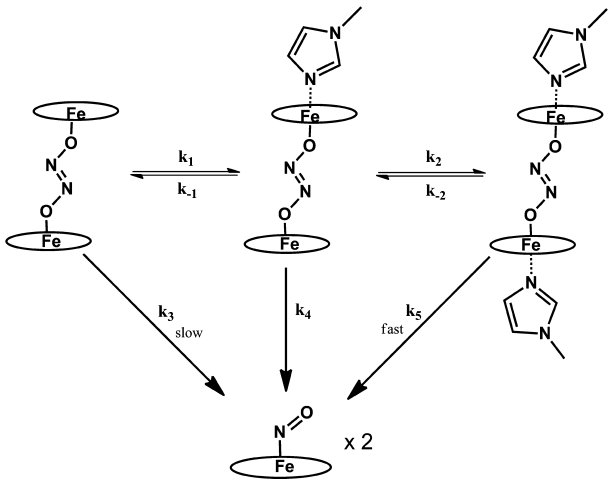

[a]Decomposition via k_3 is observed to be slow in comparison to decomposition via k_5.

to the nitrosyl product is achieved after only 80 min in the presence of a 13-fold molar excess of MI (see Figure S15 in the SI), compared to an estimated 6 h for $\{[Fe(OEP)]_2(\mu\text{-}N_2O_2)\}$ alone. This result was also confirmed by absorption spectroscopy at 30 °C in the presence of various MI equivalents. Figure 10 shows the rate constant dependence of [Fe(OEP)(NO)] formation on the MI concentration, giving a maximum rate constant of about 1.2×10^{-3} s^{-1} when MI is in >500 molar

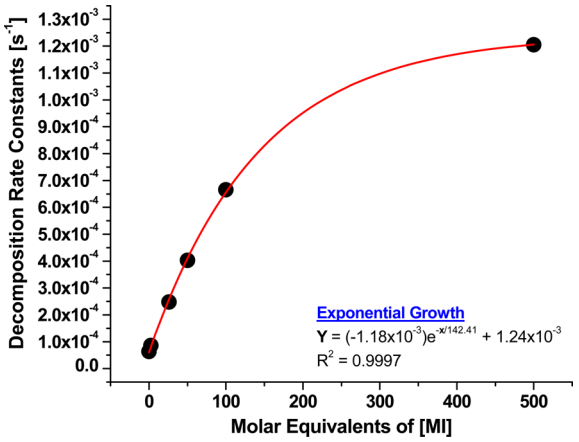

Figure 10. Dependence of the decomposition rate constants (k_{obs}) of $\{[Fe(OEP)]_2(\mu\text{-}N_2O_2)\}$ on the molar equivalents of MI. Experiments were performed at 30 °C in toluene.

excess [corresponding to a 10% reduction of the free-energy barrier (about 18 kcal mol^{-1}) compared to the five-coordinate case, according to transition state theory]. Note that, because of the overlapping signals in the absorption spectra, these rate constants should be considered as estimates. Nevertheless, the data show clearly that a saturation behavior is observed at higher MI concentrations, implying equilibrium effects upon MI addition. On the basis of these findings, it is likely that the most rapid decomposition occurs via an unstable bis(imidazole) complex, where MI binds axially across the N_2O_2-bridged complex (right side of Scheme 3). Here, equilibrium binding of MI disfavors complete formation of this bis(imidazole) adduct, only reaching complete formation at a large molar excess of MI. We attempted to simulate the kinetic data to obtain an estimate for the binding constant of MI to the hyponitrite-bridged dimer, but this is greatly complicated by the fact that the $\{[Fe(OEP)]_2(\mu\text{-}N_2O_2)\}$ complex and the corresponding mono- and bis-MI adducts cannot be distinguished spectroscopically. Our rudimentary data simulations (see the SI) estimate the MI binding constant to about 10^4 M^{-1}, but this value certainly has large error bars. Note that, at relatively high equivalents of MI (>100 equiv), NO is also displaced from the product complex [Fe(OEP)(NO)] to yield the corresponding six-coordinate ferrous bis(imidazole) complex $[Fe(OEP)(MI)_2]$, consistent with previous reports (discussed in refs 22, 63, and 64). This reaction is also observed in our EPR experiments where the [Fe(OEP)(NO)] product can be seen to disappear in the presence of >100 equiv of MI (see Figure S16, bottom, in the SI).

Interestingly, even at these high MI concentrations, no displacement of the hyponitrite ligand in $\{[Fe(OEP)]_2(\mu\text{-}N_2O_2)\}$ by imidazole is observed, which would lead to the formation of a mononuclear low-spin ferric bis(imidazole) complex that can easily be detected by EPR. This ligand displacement reaction, if it occurred, would be expected to be much faster than decomposition of the dimer into $[Fe(OEP)(NO)]$. The fact that no significant amount of a low-spin ferric complex is formed, as is evident by EPR, therefore provides direct evidence that the hyponitrite ligand is inert against displacement by MI, which is somewhat unexpected. The small amount of a low-spin ferric complex observed by EPR, as shown in Figure S15 in the SI, is, in fact, due to the mononuclear high-spin ferric impurity in the bulk $\{[Fe(OEP)]_2(\mu\text{-}N_2O_2)\}$ sample as described above, which binds MI within the mixing time of the solutions and gives rise to a weak EPR signal of appropriate intensity. This species decays over time because of slow reduction by excess MI to yield an EPR-silent, ferrous bis(imidazole) complex, which has been observed previously (cf. Figure S15, top, in the SI).[65]

Given that the hyponitrite bridge is O-bound in $\{[Fe(OEP)]_2(\mu\text{-}N_2O_2)\}$, there are several potential pathways leading to the observed nitrosyl product. The most likely pathways are sketched in Scheme 2 and involve either (i) direct breaking of the N−N bond of hyponitrite, leading to two O-bound isonitrosyl [Fe(OEP)(ON)] complexes,[48,66] which rapidly isomerize to the energetically favored N-bound isomer (pathway A), or (ii) isomerization of $\{[Fe(OEP)]_2(\mu\text{-}N_2O_2)\}$, leading to an N-bound hyponitrite bridge followed by N−N bond cleavage to yield the observed [Fe(OEP)(NO)] product (pathway B). In order to further elucidate the mechanism of overall N−N bond cleavage resulting in the formation of [Fe(OEP)(NO)], DFT calculations were employed.

dx.doi.org/10.1021/ic5002573 | Inorg. Chem. 2014, 53, 6398−6414

5. Reactivity and Decomposition of {[Fe(OEP)]$_2$(μ-N_2O_2)} Explored by DFT. *Spin-State Energetics and General Considerations.* Full optimization of {[Fe(OEP)]$_2$(μ-N_2O_2)} was performed at the BP86/TZVP theory level for both the S = 3 and 5 spin states (see section 3). Unfortunately, despite some effort, we were not able to generate optimized structures for the corresponding, broken-symmetry (antiferromagnetically coupled) systems. As mentioned above, the broken-symmetry wave function collapsed quickly into closed-shell solutions in all cases, even during simple single-point calculations. However, given that the exchange coupling constant between the iron centers is only about −1 to −2 cm^{-1}, the energy differences resulting from the exchange coupling are <0.1 kcal mol^{-1} (1 cm^{-1} = 0.003 kcal mol^{-1}) and, hence, insignificant for the reactivity of the complex investigated here.

With BP86/TZVP, the experimentally observed intermediate-spin (S = $^3/_2$) state of the iron centers, represented here by the S = 3 model, is predicted to be 18.5 kcal mol^{-1} lower in energy than the S = 5 state with S = $^5/_2$ high-spin iron centers. Single-point energies calculated with B3LYP/TZVP, on the other hand, favor the S = 5 state by 5.8 kcal mol^{-1}. However, because hybrid functionals like B3LYP tend to overly stabilize high-spin states [due to the added exact Hartree−Fock (HF) exchange] as reported in the literature, this result is not inconsistent with the iron centers being in the S = $^3/_2$ state in the experimental ground state of the complex.[67] Analogous calculations were applied to the porphine-approximated complex {[Fe(P)]$_2$(μ-N_2O_2)} to test whether the porphine approximation is valid for total energy calculations. With BP86/TZVP, the S = 3 state is now favored by 18.8 kcal mol^{-1}, whereas B3LYP/TZVP again shows a preference for the S = 5 state by 6.5 kcal mol^{-1}. These energy differences are identical within error to those obtained for the full complex and again emphasize that the porphine approximation can successfully be applied to the complex to investigate the properties and reactivity of the central Fe−N_2O_2−Fe unit. The stabilization of high-spin states by hybrid functionals correlates roughly with the amount of exact exchange added (for a given functional). Correspondingly, when the amount of HF exchange in B3LYP is reduced from 20% to 15% (in B3LYP*), the S = 3 and 5 states of the O-bound dimer become isoenergetic (energy difference: 0.1 kcal mol^{-1}), again emphasizing the challenges that DFT faces in determining the spin states of transition-metal complexes and the great sensitivity of the spin-state energetics to exact exchange.

Energy and Free-Energy Profiles for Decomposition of {[Fe(OEP)]$_2$(μ-N_2O_2)}. In order to better understand the experimentally observed decomposition of {[Fe(OEP)]$_2$(μ-N_2O_2)} into [Fe(OEP)(NO)], the DFT methodology tested above was used. B3LYP, B3LYP*, O3LYP, O3LYP*, and TPSSH single-point calculations on the BP86/TZVP-optimized structures were applied to investigate this. Although B3LYP/631G*-optimized structures are more accurate for the hyponitrite complex as described above, this method is inferior for the calculations on the nitrosyl product complexes.[21] Therefore, using BP86/TZVP-optimized structures is overall the best compromise to study the decomposition of the hyponitrite complex.

Compared to {[Fe(P)]$_2$(μ-N_2O_2)} in the S = 3 state, the S = $^1/_2$ [Fe(P)(NO)] product complex is located 8.6 kcal mol^{-1} lower in energy with B3LYP/TZVP, as shown in Figure 11. Hence, decomposition of {[Fe(OEP)]$_2$(μ-N_2O_2)} into [Fe(OEP)(NO)] is an exothermic reaction, which poses the question of why this reaction is so slow. This observation can be explained when the intermediates of the decomposition reaction are considered.

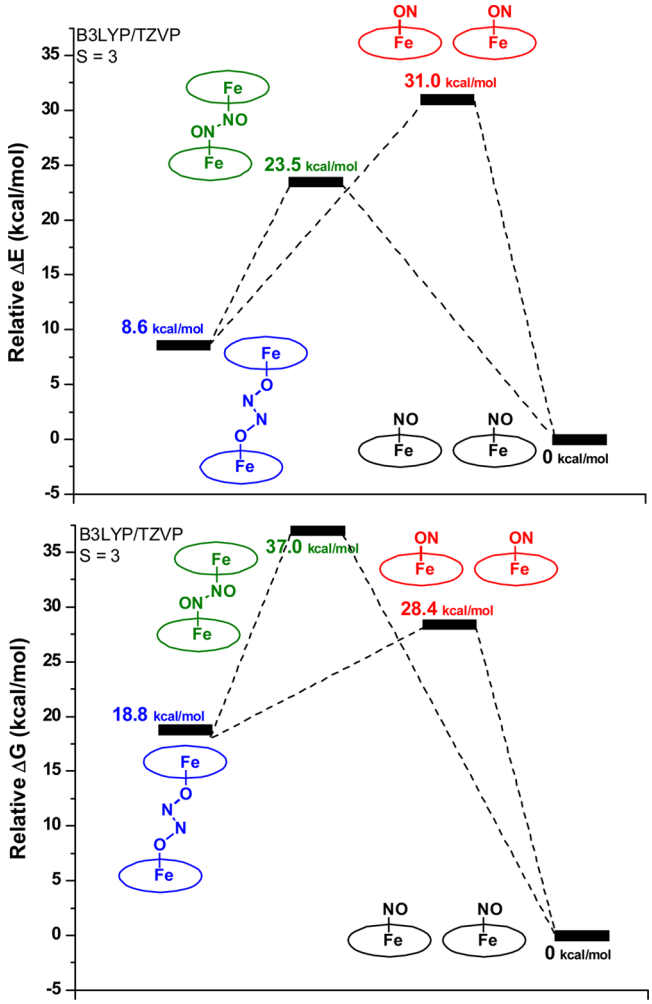

Figure 11. Calculated relative energies (top) and free energies (bottom) for the decomposition of {[Fe(OEP)]$_2$(μ-N_2O_2)} for the S = 3 spin state. Structures of the O- and N-bound isomers of {[Fe(P)]$_2$(μ-N_2O_2)} for the S = 3 spin state and of the nitrosyl complexes (S = $^1/_2$) were optimized using BP86/TZVP. The total energies were then obtained from B3LYP/TZVP single-point calculations on these optimized structures. Thermal corrections from the BP86/TZVP calculations were applied.

In order to address this issue, we considered the most likely decomposition pathways shown in Scheme 2 that proceed through either an N-bound hyponitrite-bridged isomer or a transient pair of O-bound heme nitrosyls.[68] Both of these intermediate states are predicted to be energetically unfavorable and exist +15 and +22 kcal mol^{-1}, respectively, above the S = 3 {[Fe(P)]$_2$(μ-N_2O_2)} starting material (using B3LYP/TZVP; see Figure 11, top). However, when entropic corrections are included, pathway A (see Scheme 2) with the isonitrosyl intermediate becomes favored with a barrier of about +10 kcal mol^{-1}, compared to pathway B, which shows a barrier of about +18 kcal mol^{-1}, as shown in Figure 11, bottom. This is, of course, not surprising because fragmentation of the hyponitrite-bridged dimer into two monomers should provide a stabilization of about 10 kcal mol^{-1} in free energy (at room temperature) originating from the entropy gain due to the added translational degrees of freedom of the new molecule

dx.doi.org/10.1021/ic5002573 | Inorg. Chem. 2014, 53, 6398−6414

created. Accordingly, the free-energy difference between the $\{[Fe(OEP)]_2(\mu\text{-}N_2O_2)\}$ reactant complex and the two [Fe(OEP)(NO)] product molecules increases to +18.8 kcal mol^{-1}, leading to a dramatically larger driving force for this decomposition then estimated from the ΔE values in Figure 11, top. Using B3LYP*/TZVP single-point energies as shown in Figure S18 in the SI, similar free-energy barriers are calculated, again with a preference for pathway A, which in this case has a lower barrier for hyponitrite decomposition by 7 kcal mol^{-1}. In order to further investigate the method dependency of these decomposition barriers, we also performed O3LYP, O3LYP*, and TPSSH single-point calculations (with TZVP). The resulting free-energy barriers are plotted in Figure 12.

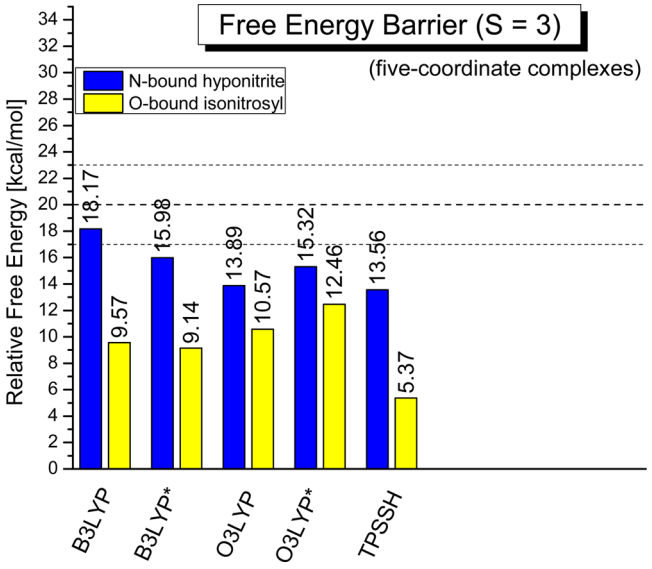

Figure 12. Calculated free-energy barriers for the decomposition of the O-bound hyponitrite complex $\{[Fe(OEP)]_2(\mu\text{-}N_2O_2)\}$ for the S = 3 spin state. Structures of the O- and N-bound isomers of $\{[Fe(P)]_2(\mu\text{-}N_2O_2)\}$ for the S = 3 spin state and of the nitrosyl complexes ($S = {}^1/_2$) were optimized using BP86/TZVP. Total energies were then obtained from B3LYP, B3LYP*, O3LYP, O3LYP*, and TPSSH single-point calculations (with TZVP) on these optimized structures. Thermal corrections from the BP86/TZVP calculations were applied.

These results lead to a dilemma: whereas in all cases the isonitrosyl pathway is preferred, the average energy barrier calculated for this pathway (about 10 kcal mol^{-1}) is too low compared to the experimental value of about 20 kcal mol^{-1}, determined kinetically. This value is actually in better agreement with the hyponitrite pathway, which shows an average energy barrier of about 16 kcal mol^{-1}. For the S = 5 hyponitrite complex, all free-energy barriers are larger, as shown in Figure S21 in the SI. This is due to the fact that the hybrid functionals overly stabilize the O-bound hyponitrite complex in the S = 5 state (see above), which then generally increases the free-energy barriers for both pathways in Scheme 2. The spin-state change that occurs along the hyponitrite decomposition pathway (generating the $S = {}^1/_2$ nitrosyl product) makes this reaction particularly sensitive to spin-state energetics, which are generally not well described by DFT (see the discussion above). Therefore, no unambiguous conclusion can be drawn about the mechanism of [Fe(OEP)(NO)] formation from $\{[Fe(OEP)]_2(\mu\text{-}N_2O_2)\}$, based on these DFT results alone. Calculations to identify the actual transition states for this reaction will be performed in future studies to further elucidate the reaction mechanism.

Evaluation of Potential Steric Hindrance. Because the calculations summarized in Figure 11 are based on the porphine approximation, we performed additional calculations on the complete molecule $\{[Fe(OEP)]_2(\mu\text{-}N_2O_2)\}$ to determine whether formation of the N-bound hyponitrite isomer (Scheme 2, pathway B) could be further hindered by unfavorable steric interactions, because the distance between the porphyrin rings is distinctively smaller in this species. Using the porphine approximation, DFT calculations predict a heme−heme distance of 6.9 Å for the crystallographically observed O-bound hyponitrite isomer and 5.7 Å for the corresponding N-bound isomer. The energy difference between the O- and N-bound S = 3 complexes within the porphine approximation is about 15 kcal mol^{-1} with B3LYP/TZVP (Figure 11, top). For the complete molecule, this energy difference increases by about 4 kcal mol^{-1} (B3LYP/TZVP), indicating that steric effects only have a small effect on the reaction energies. However, adding this energy to the average calculated free-energy barrier for $\{[Fe(OEP)]_2(\mu\text{-}N_2O_2)\}$ decomposition as discussed above leads to an estimated energy barrier for pathway B in Scheme 2 of about 20 kcal mol^{-1}, which is in excellent agreement with experiment. In summary, our DFT results somewhat favor $\{[Fe(OEP)]_2(\mu\text{-}N_2O_2)\}$ decomposition following pathway B (via the N-bound hyponitrite complex) because of the good match with the experimentally determined free reaction energy, but the competing isonitrosyl pathway cannot be ruled out in the absence of calculated transition states.

DISCUSSION

In this paper, the spectroscopic and physical properties, electronic structure, and novel decomposition reaction of the unique hyponitrite-bridged dimer $\{[Fe(OEP)]_2(\mu\text{-}N_2O_2)\}$ are presented. EPR data indicate that the two ferric iron centers in this complex are magnetically coupled, leading to a ground state that is EPR-silent at low temperature. The exact magnetic properties of the ground state of $\{[Fe(OEP)]_2(\mu\text{-}N_2O_2)\}$ are revealed by SQUID measurements, showing that this compound contains two intermediate-spin ($S = {}^3/_2$) ferric iron centers that are weakly antiferromagnetically coupled across the hyponitrite bridge. This result is also supported by low-temperature MCD measurements. Analysis of the molecular orbitals of the complex indicates that the strongest component of this exchange coupling comes from π donation from an occupied π^* orbital of hyponitrite, orthogonal to the ONNO plane, into the appropriate t_{2g}-type d orbitals of iron(III), as shown in Figure S24 in the SI. This hyponitrite π^* orbital is mostly located on the terminal oxygen atoms of the hyponitrite dianion and could therefore also be considered to have partial lone-pair character on the oxygen atoms. The overall exchange coupling mediated by this π bond across the four-atom hyponitrite bridge is weak.

The presence of intermediate-spin, $S = {}^3/_2$, iron centers in $\{[Fe(OEP)]_2(\mu\text{-}N_2O_2)\}$ is somewhat surprising but has been observed previously for other ferric OEP^{2-} complexes with O- and N-bound ligands. This includes the five-coordinate complexes $[Fe(OEP)]ClO_4$, $[Fe(OEP)(3\text{-}ClPy)]ClO_4$ (3-ClPy = 3-chloropyridine), and $[Fe(OEP)(ONNMe_2)]ClO_4$,[69−71] which all contain $S = {}^3/_2$ iron centers. In addition to these, the bimetallic complex $\{[Fe(OEP)]_2(\mu\text{-}N_2O_2)\}$ therefore

dx.doi.org/10.1021/ic5002573 | Inorg. Chem. 2014, 53, 6398−6414

represents another rare example of a synthetic intermediate-spin ferric heme complex with axial anionic oxygen donors.

Further support for this claim comes from NRVS measurements that reveal the energetic position of the E_u-symmetric (in ideal D_{4h} symmetry) Fe−N_{pyr} stretching mode between iron and the porphyrin ring.[24] This mode is sensitive to the spin state of the iron center, as clearly shown by DFT calculations using the porphine approximation. Unfortunately, if the full OEP^{2-} ligand is included in the calculations, the agreement between the experimental NRVS data and the calculated spectra is quite poor, as previously observed (see Results and Analysis, section 3). Using NRVS data as a basis to determine the spin state of the iron centers is therefore less reliable, compared to the magnetic data.

The vibrational properties of the Fe^{III}−N_2O_2−Fe^{III} unit were further investigated using isotope labeling of the hyponitrite bridge. The most characteristic vibration of the hyponitrite dianion is the antisymmetric N−O stretch, observed at 982 cm^{-1} by IR spectroscopy. For "free" sodium hyponitrite, this mode has been reported at about 1030 cm^{-1}.[72,73] Hence, this vibration undergoes a distinct shift to lower energy in $\{[Fe(OEP)]_2(\mu\text{-}N_2O_2)\}$, indicating a weakening of the N−O bond. This is likely due to polarization of the hyponitrite molecule: by binding to two ferric hemes, the molecule is locked into the $^{-}ON{=}NO^{-}$ resonance structure with two N−O single bonds, and the negative charge localized on the coordinating oxygen atoms is then stabilized by the ferric iron centers. This is in agreement with previously reported DFT calculations.[11] In addition, we were able to identify the symmetric Fe−O stretching mode in $\{[Fe(OEP)]_2(\mu\text{-}N_2O_2)\}$ at 322 cm^{-1} from the NRVS data, which provides a benchmark for the future investigation of other iron hyponitrite complexes. DFT calculations that predict the normal modes of the hyponitrite bridge in this complex were crucial to obtaining this assignment. Unfortunately, in order to estimate the Fe−O force constant for the bound hyponitrite as a measure of the Fe−O bond strength, the position of the corresponding antisymmetric Fe−O stretch also needs to be reliably determined. This was not possible in this study.

The formation of N_2O from both the treatment of $\{[Fe(OEP)]_2(\mu\text{-}N_2O_2)\}$ with acid in solution and the thermal decomposition of this complex in a KBr disk[11] indicates that hyponitrite is a likely intermediate in NORs, which are enzymes that reduce NO to N_2O. This reactivity constitutes a general reactivity pattern for hyponitrite-bridged ferric hemes because a similar reaction is also observed for the new complex $\{[Fe(PPDME)]_2(\mu\text{-}N_2O_2)\}$ ($PPDME^{2-}$ = protoporphyrin IX dimethylester dianion; see Figure S27 in the SI). Here, we report a new reaction of the hyponitrite-bridged diiron complexes, which is the decomposition into 2 equiv of a ferrous heme nitrosyl. In the case of $\{[Fe(OEP)]_2(\mu\text{-}N_2O_2)\}$, the rate of this reaction, yielding [Fe(OEP)(NO)], is very slow in the absence of an axial base (rate constant $k_{obs} = 6.4 \times 10^{-5}$ s^{-1}), indicative of a substantial kinetic barrier for this reaction (estimated at ∼20 kcal mol^{-1} from the experimental data). However, upon addition of 1-methylimidazole (MI) as a model for His, the reaction rate constant increases until saturation is reached at a rate constant of $k_{obs} = 1.24 \times 10^{-3}$ s^{-1}. These results indicate that the presence of an axial nitrogen donor, such as the proximal His residue bound to the active site heme of bacterial respiratory NOR (NorBC), further favors formation of a heme nitrosyl rather than an O-bound hyponitrite species.

These results have mechanistic implications for the mechanism of NorBC because they shed some light on the reactivity of heme-bound hyponitrite complexes. Although much research has been performed on this enzyme and a few corresponding model systems,[1] the mechanism of this enzyme is not well understood. Scheme 1 summarizes the most important mechanistic proposals put forward to date. These can be subdivided into two principal classes: the *Trans* and *Cis* mechanisms. In the two *Cis* alternatives shown in the middle and bottom of Scheme 1, one NO molecule is bound to either the ferrous heme (the *Cis*-heme b_3 mechanism) or the ferrous nonheme iron center (the *Cis*-Fe_B mechanism) first, then activated (most likely by reduction and possibly protonation), and then reacted with the second molecule of NO. Because both heme and nonheme ferrous nitrosyls do not react with excess NO by themselves, the reductive activation step seems necessary to facilitate a *Cis* mechanism.[27] This sequence of events is somewhat analogous to the mechanism of fungal NOR (P450nor).[74−78] On the basis of previous findings in the literature, the reduction of a ferrous heme nitrosyl requires very negative redox potentials,[79−84] whereas the ferrous nonheme iron nitrosyl reduces at much more positive values. This indicates that if a *Cis*-type mechanism would be active, it would more likely follow the *Cis*-Fe_B alternative (see ref 85 for further discussion). One closely related alternative would be the direct activation of NO by the two metal centers simultaneously, which requires that NO binds in a bridging fashion between the heme and the nonheme iron center. This was recently proposed by Blomberg and Siegbahn.[4]

The generally more favored mechanism goes back to Girsch and de Vries, who proposed a *Trans*-type mechanism where each ferrous iron center would bind one molecule of NO first, followed by coupling of the two coordinated NO units to form a hyponitrite intermediate, as shown on the top of Scheme 1.[7] Work on model complexes by Collman and co-workers provides some support for this general mechanistic scenario.[6,86] Girsch and de Vries further described the N−N bond-forming step as a radical-type N−N coupling reaction. Later results have shown that ferrous heme nitrosyls indeed show a large degree of radical character on the bound NO ligand and, hence, have the proper electronic structure that is in agreement with this reactivity.[21−23,25] On the other hand, ferrous nonheme iron nitrosyls are high-spin with an $Fe^{III}NO^{-}$-type electronic structure,[87] which does not seem to be in agreement with a radical-type N−N coupling step, and this finding is further supported by model complex studies.[88] The only clear example for this type of N−N bond formation was observed for a dimeric ruthenium complex.[19]

In order to evaluate the chemical feasibility of a radical-type N−N coupling step in a more general sense, it is worth taking a step back and considering such a reactivity for simple ferrous heme nitrosyls first: because ferrous heme nitrosyls (especially in the six-coordinate case) have electronic structures that are ideally poised to show radical reactivity, these systems are the ideal test cases to determine whether such a reaction could, in principle, be feasible when a heme center is involved. Of course, we know that ferrous heme nitrosyls do *not* spontaneously dimerize according to eq 1 and that the bound NO molecule is *not* reactive toward free NO gas either. Hence, especially in light of the latter result, it seems unlikely that a ferrous heme nitrosyl in the NorBC active site would undergo a radical-type N−N bond formation with a nonheme iron nitrosyl complex. This leaves us with the more general question of why the

dx.doi.org/10.1021/ic5002573 | Inorg. Chem. 2014, 53, 6398−6414

bound NO ligand in ferrous heme nitrosyls does not show any radical reactivity. The work presented in this study provides deeper insight into this issue and clearly elucidates why the spontaneous dimerization of ferrous heme nitrosyls is, in fact, not observed experimentally.

First, our DFT calculations, summarized in Figures 11 and S17 and S18 in the SI, show that the ferrous heme nitrosyl product is thermodynamically more stable than the O-bound hyponitrite-bridged dimer by roughly 20−25 kcal mol^{-1} (with B3LYP, B3LYP*, and O3LYP*) in terms of free energy (for the $S = 3$ state of the dimer). With O3LYP and TPSSH, this free-energy difference increases to roughly 35 kcal mol^{-1}, which seems unrealistically high. The alternative N-bound hyponitrite-bridged dimer is energetically very unfavorable and is predicted to be higher in free energy by about 16 kcal mol^{-1} (see Figure 12). These values were obtained with the porphine approximation, but similar energies are calculated when the full OEP^{2-} ligand is used. *These results demonstrate that the direct dimerization of ferrous heme nitrosyls is thermodynamically unfavorable*. Importantly, the DFT calculations further allowed us to construct the potential energy surface for the ferric hyponitrite to ferrous nitrosyl conversion to explore potential intermediates of this reaction and their relative (free) energies. In this way, the DFT results were crucial in order to obtain a detailed picture of this reaction landscape.

Second, the even more striking result is the extremely high-energy barrier that is present for the dimerization of ferrous heme nitrosyls. We have observed this barrier here for the first time *indirectly* by studying the reverse reaction, i.e., the decomposition of the hyponitrite-bridged dimer into ferrous heme nitrosyls. As shown in Figure 11, there are two possible decomposition pathways for the hyponitrite-bridged dimer that lead through high-energy intermediates. First, the O-bound dimer could isomerize to the corresponding N-bound form, which, however, is (on average) about 16 kcal mol^{-1} higher in free energy. Alternatively, the direct breaking of the N−N bond in the hyponitrite-bridged dimer would lead to the formation of two O-bound ferrous heme isonitrosyls, which are 10 kcal mol^{-1} higher in free energy (see Figure 12). We note that the unstable isonitrosyl [Fe(OEP)(ON)] has been observed previously at 10 K.[48] Interestingly, the rate constant observed for the decomposition of $\{[Fe(OEP)]_2(\mu\text{-}N_2O_2)\}$ of 6.4×10^{-5} s^{-1} corresponds to a barrier of roughly 20 kcal mol^{-1} and, hence, is closer to the calculated value for decomposition via the N-bound hyponitrite intermediate. This leaves us with the dilemma that the DFT-calculated lowest-energy pathway for the decay of the hyponitrite dimer does not agree with the kinetic results. This could either indicate that there is an additional, significant barrier for decomposition via the isonitrosyl intermediates (which will be further investigated in future studies) or that the DFT calculations are simply not accurate enough. Considering the generally accepted error bars of DFT-calculated energies (±5 kcal mol^{-1}), this could also be the case; i.e., DFT could also underestimate the free energy of the isonitrosyl species (relative to the O-bound hyponitrite dimer; see below).

On the basis of these results, the energy barrier for the forward reaction, i.e., the dimerization of ferrous heme nitrosyls according to eq 1, is then larger by the thermodynamic free-energy difference between two ferrous heme nitrosyls and the O-bound hyponitrite-bridged dimer, i.e., by roughly 20−25 kcal mol^{-1} (see Figures 11 and S18 in the SI), which makes this reaction kinetically fully inhibited. Hence, it is not surprising that this reaction has not been observed experimentally. The hyponitrite dimer complexes are therefore only metastable species with a tendency to decompose into 2 equiv of ferrous nitrosyls, stabilized (or trapped) by unfavorable kinetics.

In summary, these results therefore show directly that the reverse reaction of the proposed radical-type N−N coupling is preferred and that the spontaneous coupling of two ferrous heme nitrosyls is thermodynamically unfavorable and kinetically forbidden. One could argue that, in the protein active site of NorBC, a His is bound to the heme iron center, which could change the thermodynamics and kinetics of this reaction. This is, in fact, the case according to our experiments; however, the observed change is unfavorable. Binding of MI to $\{[Fe(OEP)]_2(\mu\text{-}N_2O_2)\}$ actually leads to acceleration of the decomposition reaction by almost 2 orders of magnitude but without inducing any dimerization. This indicates that the free-energy barrier for the decomposition of the hyponitrite-bridged dimer is reduced by roughly 10% in the presence of the axial imidazole (using simple transition state theory). Because six-coordinate ferrous heme nitrosyls do not spontaneously dimerize, one can conclude that the thermodynamics of the reaction have not changed in a favorable way to promote this dimerization but that binding of imidazole mostly lowers the energy barrier, which then simply facilitates decomposition of the O-bound hyponitrite complex. So the presence of His as a proximal ligand to heme is likely not able to make the radical-type N−N coupling reaction more feasible. Vice versa, if a bridging hyponitrite should form during NorBC catalysis (for example, via a reductive coupling of two NO molecules; see below), then one could speculate that the heme might become five-coordinate in order to increase the stability of this species and to prevent N−N bond homolysis, which would be catalytically unproductive. Upon formation of a $N_2O_2^{2-}$ bridge in the NorBC active site, displacement of the heme iron toward the proximal pocket may be responsible for dissociation of the proximal His ligand in this scenario. Interestingly, a similar situation has been proposed based on enzymatic studies where spectroscopic characterization of NorBC from *Paracoccus denitrificans* indicates lability of the heme b_3 Fe−His bond.[2]

These results are further supported by DFT calculations on the spontaneous decomposition of the bis-MI-bound hyponitrite dimer where both iron centers are six-coordinate. Total energy calculations on BP86/TZVP-optimized structures show that the low-spin state of the iron centers ($S = 1$ model for the dimer) is preferred over the high-spin state ($S = 5$ model) by 10−20 kcal mol^{-1} (depending on the functional) in the six-coordinate complex $\{[Fe(P)(MI)]_2(\mu\text{-}N_2O_2)\}$. As noted before, there is a strong functional dependency of the relative energies of different spin states of a given (ferric) complex (see section 5, Spin-State Energetics and General Considerations), but in this particular case, all methods (even the hybrid functionals) considered favor the $S = 1$ state. On the basis of these results, one can safely assume that the iron centers in the six-coordinate complex are low-spin, so the following considerations are focused on the $S = 1$ model of the dimer. As shown in Figure 13, the barriers for decomposition of this complex via the isonitrosyl intermediate (pathway A in Scheme 2) are increased by 4−5 kcal mol^{-1} for all methods considered compared to the five-coordinate case, whereas experimentally, the energy barrier decreases by about 10% (or ∼2 kcal mol^{-1}) upon MI coordination. For decomposition via the N-bound hyponitrite intermediate (pathway B in Scheme 2), the energy barrier is predicted to increase by about 2 kcal mol^{-1} with

dx.doi.org/10.1021/ic5002573 | Inorg. Chem. 2014, 53, 6398−6414

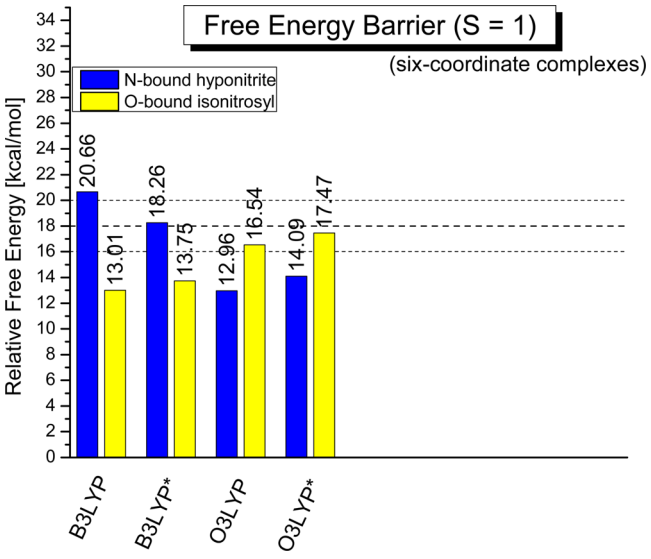

Figure 13. Calculated free-energy barriers for the decomposition of the O-bound hyponitrite complex $\{[Fe(OEP)(MI)]_2(\mu\text{-}N_2O_2)\}$ for the $S = 1$ spin state. Structures of the O- and N-bound isomers of $\{[Fe(P)(MI)]_2(\mu\text{-}N_2O_2)\}$ for the $S = 1$ spin state and of the nitrosyl complexes ($S = {}^1/_2$) were optimized using BP86/TZVP. The total energies were then obtained from B3LYP, B3LYP*, O3LYP, and O3LYP* single-point calculations (with TZVP) on these optimized structures. Thermal corrections from the BP86/TZVP calculations were applied.

B3LYP and B3LYP*, but predicted to decrease by about 1 kcal mol^{-1} with O3LYP and O3LYP* compared to the five-coordinate case (see Figure 13). This is overall in better agreement with experiment, and, in particular, the O3LYP- and O3LYP*-calculated barriers for the five- and six-coordinate cases reproduce the experimental results quite well. On the basis of these findings, it is tempting to conclude that formation of the nitrosyl complexes from the O-bound hyponitrite species occurs via the N-bound hyponitrite intermediate, but additional calculations need to be conducted (in particular, on actual transition states) to solidify this conclusion. This would also imply that there has to be an additional energy barrier present for the isonitrosyl pathway, for example, because of an unfavorable electronic reorganization for N−N bond cleavage or a change in spin state, that adds to the energy barrier for this pathway and makes it less favorable than the pathway via the N-bound hyponitrite complex. This issue is currently under investigation.

In any case, on the basis of these results, we feel that a spontaneous *Trans* radical-type N−N coupling mechanism between two ferrous nitrosyls is unlikely as a mechanistic possibility for NorBC. This, however, does not rule out the *Trans* mechanism per se because the N−N coupling step itself within the framework of this mechanism could also be facilitated by other means, for example a dipolar or redox coupling, as discussed in detail in ref 85. In the dipolar coupling scenario, the heme would become five-coordinate, which would give the complex some $Fe^{I}NO^{+}$ character.[23] This unit would then couple with the formally $Fe^{III}NO^{-}$ complex that is formed from the nonheme iron center. In the redox coupling scenario, the nonheme nitrosyl complex would be reduced by the heme, followed by coordination of the second NO to the heme center. The coupling reaction would then be facilitated by the resulting [heme-$\{FeNO\}^6$/nonheme-$\{FeNO\}^8$] intermediate. In both of these cases, the N−N coupling step would then formally correspond to the reaction of coordinated NO^+ with coordinated NO^- instead of the coupling of two neutral NO molecules. Hence, the N−N coupling would be facilitated by a charge-separation process, followed by recombination of these charges to generate the N−N bond. Alternatively, in the presence of strongly reducing metal centers, $M^{II}NO^-$ complexes have also been shown to facilitate N−N coupling [metal (M) = Fe, Ni],[16,89] and this mechanistic scenario has been considered for flavodiiron NORs. However, because the metal centers in the invoked [heme-$\{FeNO\}^7$/nonheme-$\{FeNO\}^7$] = [(heme)$Fe^{II}NO$(radical)/(nonheme)$Fe^{III}NO^-$] intermediate of the *Trans* mechanism are much less reducing, it does not seem that the same mechanism operates in NorBC.

In summary, the results presented in this study show that the spontaneous dimerization of ferrous heme nitrosyls is thermodynamically unfavorable and kinetically inhibited. This indicates that a spontaneous *Trans* radical-type N−N coupling step in the mechanism of NorBC is unlikely. All reasonable mechanistic alternatives therefore point now toward an N−N coupling step that directly involves redox chemistry and/or charge separation. In this regard, the most pressing question now pertains to the role of the nonheme iron center in the mechanism of NorBC. Further studies are on the way to address this important issue. DFT calculations were crucial in this study for the analysis of the experimental data and, in particular, for the construction of a potential energy surface for the ferric hyponitrite to ferrous nitrosyl conversion. Our results further highlight the variability in the DFT results as a function of the applied functional, demanding us (as researchers) to always compare results from different DFT methods and check for consistency in order to make strong conclusions based on DFT calculations.

■ ASSOCIATED CONTENT

Supporting Information

EPR spin quantification of the high-spin ferric impurity in $\{[Fe(OEP)]_2(\mu\text{-}N_2O_2)\}$, solid-state EPR, MCD, and IR spectra of $\{[Fe(OEP)]_2(\mu\text{-}N_2O_2)\}$, figures of DFT-optimized structures, Cartesian coordinates, DFT reaction profiles for the $S = 5$ state, kinetic simulations, and complete ref 46. This material is available free of charge via the Internet at http://pubs.acs.org.

■ AUTHOR INFORMATION

Corresponding Authors

*E-mail: grichteraddo@ou.edu.
*E-mail: lehnertn@umich.edu.

Notes

The authors declare no competing financial interest.

■ ACKNOWLEDGMENTS

APS is supported by the DOE, Basic Energy Sciences, Office of Science, under Contract DE-AC02-06CH11357. This research was supported by grants from the National Science Foundation (Grants CHE-0846235 and CHE-1305777 to N.L. and Grant CHE-1213674 to G.B.R.-A.). We further acknowledge funding from NSF grant CHE-1040008 for a SQUID instrument (University of Michigan).

■ REFERENCES

(1) Lehnert, N.; Berto, T. C.; Galinato, M. G. I.; Goodrich, L. E. In *The Handbook of Porphyrin Science*; Kadish, K. M., Smith, K. M.,

Guilard, R., Eds.; World Scientific: Hackensack, NJ, 2011; Vol. *14*, Chapter 63, p 1.
(2) Moënne-Loccoz, P. *Nat. Prod. Rep.* **2007**, *24*, 610.
(3) Wasser, I. M.; deVries, S.; Moënne-Loccoz, P.; Schröder, I.; Karlin, K. D. *Chem. Rev.* **2002**, *102*, 1201.
(4) Blomberg, M. R. A.; Siegbahn, P. E. M. *Biochemistry* **2012**, *51*, 5173.
(5) Yeung, N.; Lin, Y. W.; Gao, Y. G.; Zhao, X.; Russell, B. S.; Lei, L.; Miner, K. D.; Robinson, H.; Lu, Y. *Nature* **2009**, *462*, 1079.
(6) Collman, J. P.; Dey, A.; Yang, Y.; Decreau, R. A.; Ohta, T.; Solomon, E. I. *J. Am. Chem. Soc.* **2008**, *130*, 16498.
(7) Girsch, P.; de Vries, S. *Biochim. Biophys. Acta* **1997**, *1318*, 202.
(8) Zumft, W. G. *J. Inorg. Biochem.* **2005**, *99*, 194.
(9) Blomberg, L. M.; Blomberg, M. R. A.; Siegbahn, P. E. M. *Biochim. Biophys. Acta* **2006**, *1757*, 240.
(10) Arikawa, Y.; Onishi, M. *Coord. Chem. Rev.* **2012**, *256*, 468.
(11) Xu, N.; Campbell, A. L. O.; Powell, D. R.; Khandogin, J.; Richter-Addo, G. B. *J. Am. Chem. Soc.* **2009**, *131*, 2460.
(12) Varotsis, C.; Ohta, T.; Kitagawa, T.; Soulimane, T.; Pinakoulaki, E. *Angew. Chem., Int. Ed.* **2007**, *46*, 2210.
(13) Franz, K. J.; Lippard, S. J. *J. Am. Chem. Soc.* **1999**, *121*, 10504.
(14) Schneider, J. L.; Carrier, S. M.; Ruggiero, C. E.; Young, J. V. G.; Tolman, W. B. *J. Am. Chem. Soc.* **1998**, *120*, 11408.
(15) Arulsamy, N.; Bohle, D. S.; Imonigie, J. A.; Moore, R. C. *Polyhedron* **2007**, *26*, 4737.
(16) Wright, A. M.; Wu, G.; Hayton, T. W. *J. Am. Chem. Soc.* **2012**, *134*, 9930−9933.
(17) Kurtz, D. M., Jr. *J. Chem. Soc., Dalton Trans.* **2007**, 4115.
(18) Speelman, A.; Lehnert, N. *Acc. Chem. Res.* **2014**, *47*, 1106−1116.
(19) Arikawa, Y.; Asayama, T.; Moriguchi, Y.; Agari, S.; Onishi, M. *J. Am. Chem. Soc.* **2007**, *129*, 14160.
(20) Arikawa, Y.; Matsumoto, N.; Asayama, T.; Umakoshi, K.; Onishi, M. *Dalton Trans.* **2012**, *40*, 2148.
(21) Goodrich, L. E.; Paulat, F.; Praneeth, V. K. K.; Lehnert, N. *Inorg. Chem.* **2010**, *49*, 6293.
(22) Praneeth, V. K. K.; Näther, C.; Peters, G.; Lehnert, N. *Inorg. Chem.* **2006**, *45*, 2795.
(23) Praneeth, V. K. K.; Neese, F.; Lehnert, N. *Inorg. Chem.* **2005**, *44*, 2570.
(24) Lehnert, N.; Sage, J. T.; Silvernail, N. J.; Scheidt, W. R.; Alp, E. E.; Sturhahn, W.; Zhao, J. *Inorg. Chem.* **2010**, *49*, 7197.
(25) Berto, T. C.; Praneeth, V. K. K.; Goodrich, L. E.; Lehnert, N. *J. Am. Chem. Soc.* **2009**, *131*, 17116.
(26) Lorkovic, I. M.; Ford, P. C. *J. Am. Chem. Soc.* **2000**, *122*, 6516.
(27) Yi, J.; Morrow, B. H.; Campbell, A. L. O. C.; Shen, J. K.; Richter-Addo, G. B. *Chem. Commun.* **2012**, *48*, 9041.
(28) Ghiladi, R. A.; Kretzer, R. M.; Guzei, I.; Rheingold, A. L.; Neuhold, Y. M.; Hatwell, K. R.; Zuberbühler, A. D.; Karlin, K. D. *Inorg. Chem.* **2001**, *40*, 5754.
(29) The program *julX* written by E. Bill was used for (elements of) the simulation and analysis of magnetic susceptibility data. See: http://www.mpi-muelheim.mpg.de/bac/logins/bill/julX_en.php.
(30) Paulat, F.; Berto, T. C.; DeBeer George, S.; Goodrich, L. E.; Praneeth, V. K. K.; Sulok, C. D.; Lehnert, N. *Inorg. Chem.* **2008**, *47*, 11449.
(31) Sage, J. T.; Paxson, C.; Wyllie, G. R. A.; Sturhahn, W.; Durbin, S. M.; Champion, P. M.; Alp, E. E.; Scheidt, W. R. *J. Phys.: Condens. Matter* **2001**, *13*, 7707.
(32) Sturhahn, W. *J. Phys.: Condens. Matter* **2004**, *16*, S497.
(33) Adler, A. D.; Longo, F. R.; Kampas, F.; Kim, J. *J. Inorg. Nucl. Chem.* **1970**, *32*, 2443.
(34) Lehnert, N.; Galinato, M. G. I.; Paulat, F.; Richter-Addo, G. B.; Sturhahn, W.; Xu, N.; Zhao, J. *Inorg. Chem.* **2010**, *49*, 4133.
(35) Arulsamy, N.; Bohle, D. S.; Imonigie, J. A.; Sagan, E. S. *Inorg. Chem.* **1999**, *38*, 2716.
(36) Shaffer, C. D.; Straub, D. K. *Inorg. Chim. Acta* **1989**, *158*, 167.
(37) Cheng, L.; Lee, J.; Powell, D. R.; Richter-Addo, G. B. *Acta Crystallogr.* **2004**, *E60*, m1340.
(38) Becke, A. D. *Phys. Rev. A* **1988**, *38*, 3098.
(39) Perdew, J. P. *Phys. Rev. B* **1986**, *33*, 8822.
(40) Schaefer, A.; Horn, H.; Ahlrichs, R. J. *J. Chem. Phys.* **1992**, *97*, 2571.
(41) Schaefer, A.; Huber, C.; Ahlrichs, R. *J. Chem. Phys.* **1994**, *100*, 5829.
(42) Becke, A. D. *J. Chem. Phys.* **1993**, *98*, 1372.
(43) Becke, A. D. *J. Chem. Phys.* **1993**, *98*, 5648.
(44) Hay, P. J.; Wadt, W. R. *J. Chem. Phys.* **1985**, *82*, 270 and 299.
(45) Wadt, W. R.; Hay, P. J. *J. Chem. Phys.* **1985**, *82*, 284.
(46) Frisch, M. J. T.; et al. *Gaussian09*; Gaussian, Inc.: Pittsburgh, PA, 2009.
(47) Neese, F. *ORCA*, version 2.8; Max-Planck Institut für Bioanorganische Chemie: Mülheim/Ruhr, Germany, 2011.
(48) Cheng, L.; Novozhilova, I.; Kim, C.; Kovalevsky, A.; Bagley, K. A.; Coppens, P.; Richter-Addo, G. B. *J. Am. Chem. Soc.* **2000**, *122*, 7142.
(49) Cheng, R.-J.; Latos-Grazynski, L.; Balch, A. L. *Inorg. Chem.* **1982**, *21*, 2412.
(50) Safo, M. K.; Gupta, G. P.; Walker, F. A.; Scheidt, W. R. *J. Am. Chem. Soc.* **1991**, *113*, 5497.
(51) Lehnert, N.; DeBeer George, S.; Solomon, E. I. *Curr. Opin. Chem. Biol.* **2001**, *5*, 176.
(52) Scheidt, W. R.; Durbin, S. M.; Sage, J. T. *J. Inorg. Biochem.* **2005**, *99*, 60.
(53) Lehnert, N. In *Computational Inorganic and Bioinorganic Chemistry*; Solomon, E. I., King, R. B., Scott, R. A., Eds.; John Wiley & Sons: Chichester, U.K., 2009; p 123.
(54) Leu, B. M.; Zgierski, M. Z.; Wyllie, G. R. A.; Scheidt, W. R.; Sturhahn, W.; Alp, E. E.; Durbin, S. M.; Sage, J. T. *J. Am. Chem. Soc.* **2004**, *126*, 4211.
(55) Barabanschikov, A.; Demidov, A.; Kubo, M.; Champion, P. M.; Sage, J. T.; Zhao, J.; Sturhahn, W.; Alp, E. E. *J. Chem. Phys.* **2011**, *135*, 015101.
(56) Fujisawa, K.; Lehnert, N.; Ishikawa, Y.; Okamoto, K.-I. *Angew. Chem., Int. Ed.* **2004**, *43*, 4944.
(57) Lehnert, N.; Wiesler, B. E.; Tuczek, F.; Hennige, A.; Sellmann, D. *J. Am. Chem. Soc.* **1997**, *119*, 8869.
(58) Lehnert, N.; Wiesler, B. E.; Tuczek, F.; Hennige, A.; Sellmann, D. *J. Am. Chem. Soc.* **1997**, *119*, 8879.
(59) Paulat, F.; Lehnert, N.; Ishikawa, Y.; Okamoto, K.; Fujisawa, K. *Inorg. Chim. Acta* **2008**, *361*, 901.
(60) Lapinski, A.; Spanget-Larsen, J.; Waluk, J.; Radziszewski, J. G. *J. Chem. Phys.* **2001**, *115*, 1757.
(61) Lehnert, N. In *The Smallest Biomolecules: Diatomics and their Interactions with Heme Proteins*; Ghosh, A., Ed.; Elseviere: Amsterdam, The Netherlands, 2008; p 147.
(62) Ellison, M. K.; Scheidt, W. R. *J. Am. Chem. Soc.* **1999**, *121*, 5210.
(63) Cheng, L.; Richter-Addo, G. B. In *The Porphyrin Handbook*; Kadish, K. M., Smith, K. M., Guilard, R., Eds.; Academic Press: New York, 2000; Vol. *4*, Chapter 33, p 219.
(64) Bohle, D. S.; Hung, C.-H. *J. Am. Chem. Soc.* **1995**, *117*, 9584.
(65) Walker, F. A.; Simonis, U. In *Encyclopedia of Inorganic Chemistry*, 2nd ed.; King, R. B., Ed.; John Wiley & Sons, Ltd.: Chichester, U.K., 2005; Vol. *IV*, p 2390.
(66) Xu, N.; Yi, J.; Richter-Addo, G. B. *Inorg. Chem.* **2010**, *49*, 6253.
(67) This is due to the added exact exchange energy in hybrid functionals. For example, BP86/TZYP calculations on the ferric complex [Fe(P)Cl] predict the intermediate-spin ($S = {}^3/_2$) state to be lowest in energy, whereas B3LYP/TZVP makes the high-spin ($S = {}^5/_2$) state the ground state. The relative change in energy for these two states between BP86 and B3LYP is about 11 kcal mol^{-1}. Hence, DFT methods are not necessarily reliable for the prediction of spin states of transition-metal complexes.
(68) In theory, the complex could also decompose via an asymmetric intermediate, where hyponitrite shows a mixed O- and N-coordination, prior to N−N bond scission. However, this coordination mode would lead to very unfavorable steric interactions between the edges of the two hemes (in particular, between the ethyl substituents)

in the dimer, which would point directly at each other. For this reason, this pathway was not further considered.
(69) Axe, F. U.; Flowers, C.; Loew, G. H.; Waleh, A. *J. Am. Chem. Soc.* **1989**, *111*, 7333.
(70) Dolphin, D. H.; Sams, J. R.; Tsin, T. B. *Inorg. Chem.* **1977**, *16*, 711.
(71) Scheidt, W. R.; Geiger, D. K.; Hayes, R. G.; Lang, G. *J. Am. Chem. Soc.* **1983**, *105*, 2625.
(72) Kuhn, L.; Lippincott, E. R. *J. Am. Chem. Soc.* **1956**, *78*, 1820.
(73) Andrews, L.; Liang, B. *J. Am. Chem. Soc.* **2001**, *123*, 1997.
(74) Lehnert, N.; Praneeth, V. K. K.; Paulat, F. *J. Comput. Chem.* **2006**, *27*, 1338.
(75) Riplinger, C.; Neese, F. *ChemPhysChem* **2011**, *12*, 3192.
(76) Doctorovich, F.; Bikiel, D.; Pellegrino, J.; Suárez, S. A.; Larsen, A.; Martí, M. A. *Coord. Chem. Rev.* **2011**, *255*, 2764.
(77) McQuarters, A. B.; Wirgau, N. E.; Lehnert, N. *Curr. Opin. Chem. Biol.* **2014**, *19*, 82.
(78) Riplinger, C.; Bill, E.; Daiber, A.; Ullrich, V.; Shoun, H.; Neese, F. *Chem.—Eur. J.* **2014**, *20*, 1602.
(79) Olson, L. W.; Schaeper, D.; Lancon, D.; Kadish, K. M. *J. Am. Chem. Soc.* **1982**, *104*, 2042.
(80) Lançon, D.; Kadish, K. M. *J. Am. Chem. Soc.* **1983**, *105*, 5610.
(81) Choi, I.-K.; Liu, Y.; Feng, D.; Paeng, K.-J.; Ryan, M. D. *Inorg. Chem.* **1991**, *30*, 1832.
(82) Wei, Z.; Ryan, M. D. *Inorg. Chem.* **2010**, *49*, 6948.
(83) Pellegrino, J.; Hübner, R.; Doctorovich, F.; Kaim, W. *Chem.—Eur. J.* **2011**, *17*, 7868.
(84) Goodrich, L. E.; Saikat, R.; Alp, E. E.; Zhao, J.; Hu, M. Y.; Lehnert, N. *Inorg. Chem.* **2013**, *52*, 7766.
(85) Berto, T. C.; Speelman, A.; Zheng, S.; Lehnert, N. *Coord. Chem. Rev.* **2013**, *257*, 244.
(86) Collman, J. P.; Yang, Y.; Dey, A.; Decreau, R. A.; Ghosh, S.; Ohta, T.; Solomon, E. I. *Proc. Natl. Acad. Sci. U.S.A.* **2008**, *105*, 15660.
(87) Brown, C. A.; Pavlosky, M. A.; Westre, T. E.; Zhang, Y.; Hedman, B.; Hodgson, K. O.; Solomon, E. I. *J. Am. Chem. Soc.* **1995**, *117*, 715.
(88) Berto, T. C.; Hoffman, M. B.; Murata, Y.; Landenberger, K. B.; Alp, E. E.; Zhao, J.; Lehnert, N. *J. Am. Chem. Soc.* **2011**, *133*, 16714.
(89) Zheng, S.; Berto, T. C.; Dahl, E. W.; Hoffman, M. B.; Speelman, A. L.; Lehnert, N. *J. Am. Chem. Soc.* **2013**, *135*, 4902−4905.